Cimmerian metamorphism and post Mid-Cimmerian exhumation in Central Iran: Insights from in-situ Rb/Sr and U/Pb dating

Thomas Gyomlai, Philippe Agard, Laurent Jolivet, Tiphaine Larvet, Guillaume Bonnet, Jafar Omrani, Kyle Larson, Benoit Caron, Julie Noël

Journal Pre-proofs

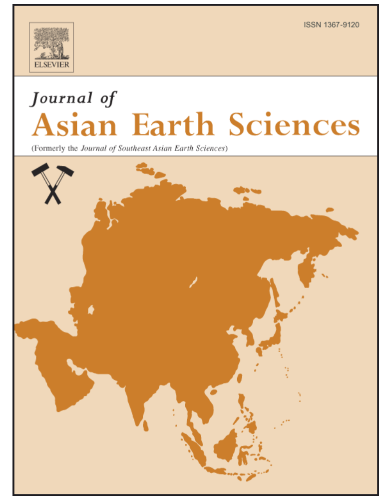

Cimmerian metamorphism and post Mid-Cimmerian exhumation in Central Iran: Insights from in-situ Rb/Sr and U/Pb dating

Thomas Gyomlai, Philippe Agard, Laurent Jolivet, Tiphaine Larvet, Guillaume Bonnet, Jafar Omrani, Kyle Larson, Benoit Caron, Julie Noël

PII:	S1367-9120(22)00165-1
DOI:	https://doi.org/10.1016/j.jseaes.2022.105242
Reference:	JAES 105242

To appear in: *Journal of Asian Earth Sciences*

Received Date:	4 December 2021
Revised Date:	23 April 2022
Accepted Date:	24 April 2022

Please cite this article as: Gyomlai, T., Agard, P., Jolivet, L., Larvet, T., Bonnet, G., Omrani, J., Larson, K., Caron, B., Noël, J., Cimmerian metamorphism and post Mid-Cimmerian exhumation in Central Iran: Insights from in-situ Rb/Sr and U/Pb dating, *Journal of Asian Earth Sciences* (2022), doi: https://doi.org/10.1016/j.jseaes.2022.105242

Cimmerian metamorphism and post Mid-Cimmerian exhumation in Central Iran: insights from in-situ Rb/Sr and U/Pb dating.

Thomas Gyomlai[1*], Philippe Agard[1], Laurent Jolivet[1], Tiphaine Larvet[1], Guillaume Bonnet[1], Jafar Omrani[2], Kyle Larson[3], Benoit Caron[1] and Julie Noël[4]

[1]Sorbonne Université, CNRS-INSU, Institut des Sciences de la Terre de Paris, ISTeP UMR 7193, 4 pl. Jussieu, Paris 75005, France

[2]Geological Survey of Iran, Mehraj Bd., Tehran, Iran

[3]Department of Earth, Environmental and Geographic Sciences, University of British Columbia, Okanagan, Kelowna, BC VIV 1V7, Canada

[4]OSU Ecce Terra, UMS 3455, CNRS and Sorbonne Université, Paris, France

*Corresponding author (email: thomas.gyomlai@sorbonne-universite.fr; postal address: ISTeP - 4, Place Jussieu 75252 PARIS Cedex 05, France)

Abstract

The pre-Alpine evolution of the Tethyan domains between Gondwana and Laurasia, and in particular that of the Cimmerian continental blocks, remains poorly constrained. Central Iran is a key area to constrain the closure of the Paleotethys and the collision of Laurasia with the Cimmerian blocks drifted from Gondwana. The present study provides a combined metamorphic and geochronologic approach focused on two areas of Central Iran: the Kashmar-Kerman Tectonic Zone (KKTZ) and the Jandaq area, whose tectonometamorphic units are affected low- to middle-pressure high-temperature metamorphism. We performed in-situ texturally constrained U/Pb dating on titanite and Rb/Sr dating on mica to quantify the timing and intensity of burial and exhumation of these metamorphic rocks. Results show that metamorphism in the central and eastern KKTZ (7-9 kbar; ~700°C) is synchronous or slightly postdates the Cimmerian orogeny (~190-180 Ma) and relates to the collision following the Paleotethys closure, whereas metamorphism in the Jandaq complex (12-13 kbar; ~450°C) relates to the Paleotethys subduction. Based on paleogeographic reconstructions, the KKTZ lied hundreds of kilometers south of the Paleotethys suture zone. As such, we propose that metamorphism along the KKTZ results from the closure and shortening of a rheologically weak domain located outboard of the main suture. In-situ Rb/Sr dating of biotite yields precise and accurate cooling ages (± 2-5 Ma) ranging from 170 to 140 Ma. These cooling ages document the exhumation of these terranes from the Mid-Cimmerian event onward (~170 Ma), coeval with the widespread extension distributed across Iran and thought to reflect upper plate extension above the Neotethyan subduction system.

Keywords

Central Iran; Collisional metamorphism; in-situ Rb/Sr dating; Cimmerian orogeny; Neotethys subduction

1 Introduction

Plate kinematics since the Cambrian have been dominated by the diachronous drifting and collision of Gondwana-derived continental blocks with Laurasia and the associated formation of large-scale orogenic belts, with major implications for geodynamics (Şengör, 2012), paleoclimate (Smith, 1979) and ore formation (Metcalfe, 2021). The amalgamation of these blocks results from the opening and closure of several Tethyan oceanic domains (Suess, 1895; Stille, 1958; Flügel, 1972; Şengör, 1979): the Prototethyan oceans (which led to the Cadomian orogeny), the Paleotethys ocean (Cimmerian and Indosinian orogenies), the Mesotethys or Rheic ocean (Variscan orogeny) and the Neotethys ocean (Alpine and Himalayan orogenies). The mechanism driving this stepwise fragmentation of the Gondwana margin and later accretion onto Laurasia, similar to a 'diffuse' collision between Gondwana and Laurasia, likely relates to asthenospheric upwelling and horizontal flow below Gondwana (Ziegler, 1992; Jolivet et al., 2016). Constraining its detailed processes and exact timing is unfortunately frequently complicated by the Alpine overprint onto the geological archive of earlier orogenic structures.

Central Iran is a key area to study this dynamic evolution (Fig. 1), as it preserves a mosaic of Gondwana-derived 'Cimmerian' terranes thought to have once formed a composite continental domain – or a set of continental blocks – between the Paleotethys and the Neotethys. Central Iran is limited by several ophiolite belts (Fig. 1, e.g., Sistan, Sabzevar, Nain-Baft; Moghadam and Stern, 2015) and dissected by large-scale active faults (Walker et al., 2004), but largely escaped the Paleogene-Neogene magmatism which affected most of Iran (Fig. 1). It exposes metamorphic and magmatic rocks that preserve evidence of several major geological episodes: Panafrican/Cadomian magmatism (Rossetti et al., 2015; Hassanzadeh et al., 2008; Moghadam et al., 2017), subduction and closure of the Paleotethys, with subsequent Mesozoic tectonic activity during the Eo-, Mid- and Late-Cimmerian events (Fürsich et al., 2009b; Zanchi et al., 2009b; Wilmsen et al., 2015; Rossetti et al., 2017), and Mesozoic to present tectonics linked to the subduction of the Neotethys (Agard et al., 2011; Mattei et al., 2015; Wilmsen et al., 2021).

Unravelling the tectono-metamorphic evolution of the region is essential to elucidate the geodynamic setting and significance of these successive geological events. Metamorphic rocks, however, are relatively sparsely exposed across desert areas and/or covered by Quaternary infill (Fig. 1). Estimates of their pressure and temperature conditions, as well as absolute age data, are mostly lacking. One example is the high temperature and medium pressure (HT-MP) metamorphic event ascribed to the Cimmerian orogeny, around 220-185 Ma (Horton et al., 2008; Fürsich et al., 2009a; Wilmsen et al., 2009a; Zanchi et al., 2009a, 2015; Wilmsen et al., 2015), which is documented in Central and North-East Iran in the Kashmar-Kerman Tectonic Zone (Ramezani and Tucker, 2003; Kargaranbafghi et al., 2012), as well as in the Jandaq (Bagheri and Stampfli 2008; Berra et al. 2017) and Shotor-Kuh complexes (Rahmati-Ilkhchi et al., 2011; Malekpour-Alamdari et al., 2017). These complexes are nevertheless located hundreds of kilometers apart and away from the Paleotethys suture zone (Fig. 1), making this collisional metamorphism enigmatic. Furthermore, while the absolute ages reported for these areas (Verdel et al., 2007; Bagheri and Stampfli 2008; Rahmati-Ilkhchi et al., 2011; Masoodi et al., 2013; Tab. 1) are commonly related to the Mid-Cimmerian tectonic event (~170-168 Ma; Fürsich et al., 2009b; Wilmsen et al., 2009b,a), the nature and intensity of this event are still poorly constrained.

The present study aims to refine our understanding of the Cimmerian and subsequent Jurassic events through a combined metamorphic and geochronologic approach focused on two understudied areas of Central Iran: (1) the Kashmar-Kerman Tectonic Zone (KKTZ) and (2) the Jandaq area. In order to obtain an extensive dataset of texturally constrained ages across a vast area, we have calibrated and implemented the in-situ Rb/Sr dating on biotite and white mica combined with titanite U-Pb geochronology. Results provide insights into the timing and intensity of burial and exhumation of the investigated metamorphic rocks, as well as into the tectonics of the Cimmerian orogeny.

2 Geological context

2.1 Paleogeography of the Cimmerian blocks

The Central-East-Iranian Microcontinent (CEIM) consists of the Yazd, Tabas, and Lut continental blocks, which are separated by active strike-slip faults (Figs. 2,3). These faults are thought to rework Palaeozoic and/or older structures (Berberian and King, 1981). The CEIM belongs to the western Cimmerian blocks together with the Alborz, Sanand (or Sanandaj-Sirjan) and Afghan blocks, which were part of the Gondwana passive margin during the Early Paleozoic.

During the Late Neoproterozoic and Early Cambrian, the Prototethys (locally termed Ran ocean) is thought to have subducted beneath the northern part of Arabia, the western Cimmerian blocks and northern India (Torsvik and Cocks, 2016; Fig. 3). This is documented by the presence of extensive Cambrian andesites and trondhjemites in the western part of the CEIM (Ramezani and Tucker, 2003) and by late Neoproterozoic–Early Cambrian granitoids in Iran (Hassanzadeh et al., 2008). This active margin setting is associated with the Cadomian orogeny (Rossetti et al., 2015; Moghadam et al., 2020).

During the Early Paleozoic, the western Cimmerian blocks lied close to Arabia based on their similar paleomagnetic record (Wensink et al., 1979; Muttoni et al., 2009b) and on the nature of the basement and of the overlying sedimentary succession (Stöcklin, 1968; Stöcklin, 1974; Berberian and King, 1981; Wendt et al., 2005). A thick discontinuous and poorly deformed Cambrian to Triassic succession records the passive margin history of these blocks (Torsvik and Cocks, 2009).

Following initial rifting during the late Silurian, the Paleotethys ocean opened during the early Devonian, separating part of the Hunic terranes from the Gondwana margin (e.g., the Karakum-Turan, Pamirs, Tarim, Qiangtang, North China terranes and the various terranes which now make up southern Europe; Stampfli and Borel, 2002; Torsvik and Cocks, 2016). North of Gondwana, remnants of a north-dipping subduction of the Paleotethys Ocean below Laurasia are documented along northern Iran and in the Anarak-Jandaq zone in central Iran (Fig. 3a) :

(i) Around Mashhad (Fig. 1), remnants of an accretionary wedge marking Palaeotethys closure has been extensively studied (Stöcklin, 1974; Alavi, 1991; Boulin, 1991; Ruttner, 1993; Alavi et al., 1997; Sheikholeslami and Kouhpeyma, 2012).

(ii) Carboniferous eclogites occur in Shanderman and Rasht (Fig. 1) in the Talesh Mountains, western Alborz (Zanchetta et al., 2009; Omrani et al., 2013; Rossetti et al., 2017).

(iii) In central Iran, the Carboniferous HP-LT metamorphism of the Anarak and Jandaq Metamorphic Complexes (Bagheri and Stampfli, 2008; Zanchi et al., 2015), the Triassic forearc succession of Nakhlak (Balini et al., 2009) and the arc detrital deposition of Godar-e-Siah (Berra et al., 2017) can be framed in the same Paleotethys active margin setting (Fig. 2).

(iv) East of Mashhad, in the Fariman-Aghdarband region of NE Iran, the arc-related units of Fariman and Darreh Anjir record active subduction during the Permian, as well as during the Devonian and Carboniferous (Zanchetta et al., 2013; Moghadam et al., 2015).

(v) The arc-related succession of Aghdarband, exposed north of Fariman (Fig. 1), is also consistent with Paleotethys subduction during the Early to Middle Triassic (Ruttner et al., 1991; Zanchi et al., 2016).

The gradual opening of the Neotethys Ocean within the north-east rim of Gondwana during the Early Permian (from about 275 Ma; Domeier and Torsvik, 2014) separated a series of microcontinents and terranes (Sibumasu, Tibetan, Turkey, Alborz, Iran, Karakorum, Lut, Sanand, Afghanistan, and Pakistan) from the northern Gondwana margin (Fig. 3b). Paleomagnetic and sedimentary data indicate that these terranes, called the Cimmerian blocks, resided on subequatorial paleolatitudes during the Late Permian-Early Triassic (Muttoni et al., 2009b). The central Cimmerian terranes (e.g. central Afghanistan, Karakoram) were located northward with respect to the other Cimmerian terranes (Angiolini et al., 2003; Angiolini, 2001; Campi et al., 2005, Muttoni et al., 2009a). Whether the other Cimmerian terranes formed a single elongate continent (referred to as Cimmeria) or several distinct microcontinental blocks remains unclear. Indeed, the relative motion and potential paleolatitude difference between the western Cimmerian blocks (Alborz v. CEIM v. Sanand v. Afghan) cannot be ascertained because palaeomagnetic results are sparse and uncertainties too large (Muttoni et al., 2009b; Torsvik and Cocks, 2016).

In the Late Triassic (Fig. 3c), the closure of the Paleotethys ocean resulted in the Cimmerian Orogeny, which was defined based on mid-Mesozoic convergent plate-margin activity stretching from Bulgaria to southeastern Asia (Suess, 1895; Şengör, 1979). In Iran, it corresponds to the collision of the western Cimmerian blocks with the active margin of the Turan Terrane (Berra et al., 2007; Horton et al., 2008; Fürsich et al., 2009a; Zanchi et al., 2009a; Zanchetta et al., 2009). The Cimmerian orogeny in Iran may have comprised several diachronous collisional events between the different western Cimmerian blocks (Golonka, 2004). Inception of collision is proposed at 225 Ma (Wilmsen et al., 2009b). The shift from Middle Triassic platform carbonates to the siliciclastic rocks of the Shemshak Group (and equivalent successions) observed throughout Iran reflects the onset of an Eo-Cimmerian deformation from approximatively 220 to 185 Ma (Horton et al., 2008; Fürsich et al., 2009a; Wilmsen et al., 2009a; Zanchi et al., 2009a, 2015; Wilmsen et al., 2015). The subduction of the Neotethys below the Iranian terranes probably began in the Late Triassic or Early Jurassic, as testified by arc magmatism (Berberian and King, 1981) and eclogite formation (Davoudian et al., 2016) in the Sanandaj-Sirjan Zone. The formation of the extensional Nayband Basin (~210 Ma;

Fürsich et al., 2005; Wilmsen et al., 2009b) is thought to reflect reduced compression across the Iranian blocks due to early back-arc extension after the initiation of this subduction.

The tectonic evolution of Iran after the main Cimmerian orogeny is marked by two discrete tectonic phases: the Mid- and Late-Cimmerian events. Those events were first described in Europe (Stille, 1924; Ziegler, 1975) and corresponding unconformities in the sedimentary record were later described in Iran (Seyed-Emami and Alavi-Naini, 1990). In Iran, the Mid-Cimmerian event is defined by an unconformity on top of the Shemshak Group and is apparently confined to the Bajocian (~170-168 Ma; Fürsich et al., 2009b). This compressional event was characterized in the Alborz by rapid uplift (60 m/Myr) followed by significant subsidence possibly marking the onset of spreading in the South Caspian Basin (Fürsich et al., 2009b). This phase of rapid subsidence is observed across all of northeast Iran and is interpreted as crustal extension across rotating blocks to explain the great magnitude of relative deepening (Fürsich et al., 2009b; Wilmsen et al., 2009b,a).

A less well-constrained Late-Cimmerian event occurred during the Late Jurassic (~145 Ma), mostly across Central Iran (Zanchi et al., 2009b; Wilmsen et al., 2015, 2021). This event is possibly related to the opening and closure of the Iranian back-arc basins at the rear of the large-scale subduction zone of the Neotethys (Rossetti et al., 2010; Agard et al., 2011). The opening and closure of these small oceanic basins was accompanied by the activity of the Great Kavir-Doruneh Fault (Javadi et al., 2013, 2015) and by significant lateral displacements and block rotations.

One of the consequences of these post-Cimmerian block movements/rotations could be the large-scale translation (~500 km) of the Nakhlak, Anarak and Jandaq complexes from the

Paleotethys suture to the interior of Central Iran (Fig. 2; Bagheri and Stampfli 2008; Zanchi et al. 2015; Berra et al. 2017). These complexes, with Eurasian paleobiogeographic affinities and active margin imprints, are now exposed between the Great Kavir Doruneh Fault and the Palaeozoic-Triassic successions of Gondwana affinity of the Yazd block. Initial palaeomagnetic data indicated that the CEIM reached its actual position after a 135° anticlockwise rotation (Davoudzadeh and Weber-Diefenbach, 1987; Soffel et al., 1996). More recently, however, Mattei et al. (2015) proposed a two-stage anticlockwise rotation of about 85° since the Jurassic, with a first stage occurring during the Early Cretaceous and a second one after the Middle–Late Miocene. These rotations seem confined to the CEIM and do not extend to the other tectonic provinces of Iran. The stratigraphy and facies distribution show that the Yazd Block was emergent during most of the Jurassic period and that the marine influence increased from the Tabas block to the Lut block (Fig. 3; Dercourt et al. 1986; Fürsich et al. 2003; Wilmsen et al. 2003, 2005, 2010). On this basis, Mattei et al. (2015) proposed that the Yazd, Lut and Tabas blocks were oriented WSW–ENE during the Late Jurassic with the Lut Block facing the Neotethys Ocean to the south and southeast (see Fig. 3c). Lastly, central Iran was affected, from ~30 Ma onwards, by the Zagros orogeny marking the closure of the Neotethys and resulting in overprinting deformation across Iran (e.g. Alborz and Kopeh Dagh; Agard et al. 2011; Ballato et al., 2011; Jentzer et al. 2017).

2.2 Studied areas

This study focuses on the metamorphism related to the subduction and collision of the Paleotethys. For the sake of clarity, geological contexts for the Rasht, Anarak and Shotor-Kuh complexes were metamorphism related to the Paleotethys occurred are presented in the supplementary section.

2.2.1 Kashmar-Kerman Tectonic Zone

The Kashmar–Kerman Tectonic Zone (KKTZ) separates the Yazd block from the Tabas block (Haghipour et al., 1977a; Ramezani and Tucker, 2003). Unlike in those blocks, Neoproterozoic and Lower Paleozoic rocks are well exposed in the KKTZ, including several metamorphic complexes overlain by Mesozoic and Cenozoic sedimentary units. Ramezani and Tucker (2003) distinguished three lithotectonic domains in the KKTZ separated by large strike-slip faults (Western, Central and Eastern; Fig. 4):

A Western domain, bounded to the west by the Chapedony fault and to the east by the Neybaz-Chatak fault, which comprises the Chapedony complex and several magmatic intrusions (e.g. the Koshoumi granite and Daranjir Diorite) dated between 40 and 49 Ma (Ramezani and Tucker, 2003; Verdel et al., 2007). The Chapedony Metamorphic Complex includes high-grade gneisses, migmatites and anatectic granites (Haghipour et al., 1977a) with peak metamorphism at approximately 46 Ma (Ramezani and Tucker, 2003) and Ar-Ar ages for various minerals ranging from 40 to 48 Ma (Verdel et al., 2007; Kargaranbafghi et al., 2012, 2015). Late- to post-metamorphic intrusion of granite-diorite plutons into the complex were dated at approximately 45 Ma (U-Pb zircon; Ramezani and Tucker, 2003). Peak P–T conditions were estimated at 3 kbar and 650–750 °C (Kargaranbafghi et al., 2015) using the Al-in-hornblende barometer (Anderson and Smith, 1995) and the amphibole–plagioclase thermometer (Holland and Blundy, 1994). The Ar-Ar ages, together with published U–Pb zircon and U–Th/He apatite and zircon ages (Tab. 1), imply rapid cooling from 750°C to 60°C of the Chapedony complex between 49 and 30 Ma (Kargaranbafghi et al., 2015). The Chapedony complex was interpreted as a core complex exhumed below the central domain by the east deepening normal Neybaz-Chatak fault (Ramezani and Tucker, 2003; Verdel et al., 2007; Kargaranbafghi et al., 2012, 2015; Fig. 4). The Chapedony core complex is interpreted as the result of magmatic underplating and crustal extension associated with a regional magma flare-up during the Eocene (Verdel et al., 2011; Kargaranbafghi et al., 2015).

A Central domain, between the Neybaz-Chatak and Posht-e-Badam faults (Fig. 4). It is composed of the Posht-e-Badam complex, magmatic intrusions such as Chamgoo and Anarg granodiorites or the Esmailabad Granite (Ramezani and Tucker, 2003), a Cambrian volcano-sedimentary unit and Permian to Paleogene-Neogene sedimentary units. The Posht-e-Badam Complex is made of an association of greenstones, schists, gneisses, amphibolites and marbles. The complex is severely disrupted by thrusting, as also evidenced by large-scale folded marbles, and intrusion of granitoid plutons. The Esmailabad Granite is dated at 218 ± 3 Ma (2σ) and the Chamgoo Granodiorite at 213.5 ± 0.5 Ma (2σ). These intrusions, with distinctive peraluminous character and high concentrations in LILE (Rb and Cs), were interpreted as anatectic or collisional granitoids (Ramezani and Tucker, 2003) and ascribed to the Cimmerian orogeny. No Late Triassic magmatic intrusions have been described in the KKTZ outside of this Central Lithotectonic Domain. The medium-grade metamorphism within the Posht-e-Badam complex was dated at 219.2 ± 2.4 Ma (2σ; Ar-Ar hornblende; Kargaranbafghi et al., 2012) and also attributed to the Cimmerian orogeny.

An Eastern lithotectonic domain, between the Posht-e-Badam and the Kalmard Fault, comprises the Tashk, Boneh-Shurow and Sarkuh complexes, magmatic intrusions (including the Ariz and Polo granodiorites or the Zarigan, Douzakh-Darreh and Sefid trondhjemitic intrusions), a Cambrian Volcano-sedimentary unit and Paleozoic and Mesozoic sedimentary units.

The Tashk Complex comprises weakly metamorphosed sedimentary and volcaniclastic rocks (Haghipour et al., 1977a) deposited from the Late Neoproterozoic to Early Cambrian. Ramezani and Tucker (2003) constrained the depositional age of the formation between 627 Ma (youngest zircon population in a tuffaceous rock) and 533 Ma, which corresponds to the oldest known magmatic intrusion (i.e. the Ariz Granodiorite). The Tashk Formation was deposited in a marginal marine environment with volcanic influence and is unconformably overlain by Permian and Triassic shallow-marine carbonates.

The Sarkuh Complex is composed of marble and medium grade metamorphic rocks such as garnet-staurolite-andalusite schists, micaschists, amphibolites and metavolcaniclastics later intruded by felsic porphyries. This complex is poorly studied and, to the authors' knowledge, no geochronological data are available.

The Boneh-Shurow complex was divided in three areas for clarity, with the northern area around the city of Posht-e-Badam, the central area in the Eskamblo mountain and the southern area in the Posht-e-Shorkh mountain (Fig. 4). The Boneh-Shurow Metamorphic Complex is composed of several lithologies such as:

(i) Mylonitic orthogneiss (Haghipour et al., 1977a) or protogneiss (Ramezani and Tucker, 2003), which is the dominant lithology in the northern area, yielding a U-Pb zircon age for the protolith of 544 ± 7 Ma (2σ).

(ii) Micaschist, phyllite, slate, metasandstone, calcsilicate and carbonate rocks with detrital U-Pb zircon ages from 602 Ma to 617 Ma (Ramezani and Tucker, 2003).

(iii) Garnet-amphibolite rocks including mainly hornblende, garnet, plagioclase and biotite. The peak metamorphism was dated at 547.6 ± 2.0 Ma (2σ; U-Pb zircon; Ramezani and Tucker, 2003).

(iv) Quartz-diorite intrusions emplaced at 547.0 ± 2.5 Ma (2σ; U-Pb zircon; Ramezani and Tucker, 2003).

(v) Mylonitic schists, dominant lithology in the southern area.

Kargaranbafghi et al. (2012) proposed that the Boneh-Shurow complex was affected by low-grade metamorphism during a late stage of the Cimmerian orogeny (Ar-Ar white mica; 140.8 ± 0.6 Ma; 2σ). The formation of a Jurassic core-complex below an east-dipping normal fault was described in the Central area (Masoodi et al., 2013; Soleimani et al., 2021) (Fig. 4).

Ramezani and Tucker (2003) proposed that the granite-tonalite intrusions and the Boneh-Shurow granitic orthogneiss, based on their magmatic-arc affinity and similar ages (U-Pb zircon; 533 ± 1 and 542 ± 9 Ma respectively; 2σ), belong to a similar Late Neoproterozoic-Early Cambrian magmatic event. The granite-tonalite intrusions are intrusive in the volcano-sedimentary Tashk complex and may represent a shallow level of a volcanic arc. The Boneh-Shurow complex, which comprises terrigenous, semi-pelitic and carbonaceous protoliths, is more likely a distal part of this Late Neoproterozoic-Early Cambrian magmatic arc complex. The presence of the Cambrian Volcano-Sedimentary Unit also supports the existence of a magmatic-arc setting dated at approximately 528

Ma (U-Pb zircon; Ramezani and Tucker, 2003). Finally, the trondhjemite intrusions of the Cambrian Leucogranite Suite were dated at 525 ± 7 Ma (2σ; U-Pb zircon) and show evidence for the Early Cambrian subduction of young oceanic crust and possibly the termination of arc magmatism (Ramezani and Tucker, 2003). This Neoproterozoic-Early Cambrian magmatic arc complex, which was interpreted as marking the Prototethyan active margin of Gondwana (Ramezani and Tucker, 2003), was recently reappraised as the subduction zone of the Ran ocean (which predated the Cadomian orogeny; Torsvik and Cocks, 2016). The impact of the Cimmerian orogeny on this domain has been studied by Masoodi et al. (2013) who proposed three deformation stages: (1) a D1-1 dextral strike-slip event with an early Jurassic cooling phase (before 186 Ma, Eo-Cimmerian); (2) a Middle Jurassic D1-2 extensional event with a top-to-NE sense of shear on low-angle normal faults (Mid-Cimmerian); (3) a D2 reverse shear event occurring during the Early Cretaceous (Late-Cimmerian).

2.2.2 Jandaq complex

The Jandaq Metamorphic Complex (JMC; Bagheri and Stampfli 2008; Berra et al. 2017) is located immediately south of the Great Kavir Fault and includes large bodies of amphibolites, garnet- staurolite-mica-bearing schists and gneiss intruded by pegmatites (Fig. 2; Berra et al. 2017). The JMC is juxtaposed against the Arusan Ophiolite, which was intruded by Jurassic granitoids (Aistov et al., 1984). Radiometric ages yield Carboniferous (333-318 Ma for Ar-Ar dating in white mica) and Jurassic ages (163.86 ± 1.76 Ma and 156.56 ± 33.15 Ma for Ar-Ar dating in a muscovite and in a hornblende respectively; 2σ), whereas the pegmatites have a Late Triassic age based on a U-Pb single crystal zircon dating (215 ± 15 Ma; 2σ; Bagheri and Stampfli, 2008).

Similarities in lithologies between the Posht-e-Badam complex and the Jandaq metamorphic complex were pointed out by Bagheri and Stampfli (2008), and with the Boneh-Shurow Complex by Ramezani and Tucker (2003).

3 Analytical methods

3.1 Electron probe microanalysis (EPMA) and scanning electron microscope (SEM) analysis

EPMA and SEM were carried out at CAMPARIS (SU-IPGP, Paris, France) using the CAMECA SX-100 and CAMECA SX-FIVE instruments and the data reducing method of Pouchou and Pichoir (1991). Analytical conditions for spot analysis were 15 kV accelerating voltage and 10 nA specimen current with a dwell time of 50 ms and a beam size of 2 µm. Fe_2O_3, $MnTiO_3$, diopside, Cr_2O_3, K-feldspar, anorthite and albite were used as standards. Mineral abbreviations are after Whitney and Evans (2010).

3.2 In-situ titanite U/Pb geochronology

Titanite U-Pb petrochronology was carried out via laser ablation inductively coupled plasma mass spectrometry (LA-ICP-MS/MS) in the Fipke Laboratory for Trace Element Research (FiLTER) at the University of British Columbia, Okanagan using a Teledyne Analyte 193 nm Excimer laser coupled to an Agilent 8900 triple quadrupole ICP-MS. All grains were analyzed in thin sections to preserve textural relationships. Spot analyses were carried out across 5 analytical sessions using a 40-micron diameter laser spot with a repetition rate of 6 Hz and fluence of 4.00 J/cm^2. The Ar sample gas (0.9 L/min) and He carrier gas (0.35 L/min) were mixed before the plasma using an in-house glass mixing valve/signal smoothing device. The analytical setup was optimized for maximum signal using the ^{238}U/^{232}Th ratio of the reference material 'NIST610' to within 3% of the certified value. Each spot was pre-ablated with two laser bursts followed by a 25 second delay before 25 seconds of ablation. Isotopic data from titanite were normalized to repeat analyses of the titanite reference material 'MKED' (^{206}Pb/^{238}U age of 1517.32 ± 0.32 Ma, Spandler et al., 2016) with 'Mount McClure' (^{207}Pb/^{235}U age of 523.26 ± 1.27 Ma, Schoene and Bowring, 2006) used as a secondary reference material to verify the analytical procedure. Down-hole element fractionation and instrument drift were monitored based on the primary reference material and corrected for using the Iolite software package v.4.5 (Paton et al., 2010, 2011). Analyses of the Mount McClure reference material as unknowns yielded lower intercept dates of 526 ± 5 (MSWD = 1.0, n = 10/11), 525 ± 10 (MSWD = 1.7, n = 7/9), 534 ± 7 (MSWD = 2.1, n = 8/10), 535 ± 4 (MSWD = 1.2, n = 12/13), 525 ± 5 (MSWD = 0.87, n = 12/14) in Tera-Wasserburg space, all well within 2% uncertainty of the accepted value. Up to 1.5% additional uncertainty was added quadratically to the ^{206}Pb-^{238}U ratios and up to 0.5% to the ^{207}Pb-^{206}Pb ratios of all analyses as indicated by the overdispersion of ratios from the secondary reference materials from the same analytic sessions.

Trace element concentrations were measured with the U-Pb isotopes for each spot. A dwell time of 10 ms was used for ^{29}Si, ^{31}P, ^{43}Ca and ^{90}Zr while a dwell time of 15 ms was used for ^{49}Ti, ^{89}Y, ^{93}Nb, ^{139}La, ^{140}Ce, ^{141}Pr, ^{146}Nd, ^{147}Sm, ^{153}Eu, ^{157}Gd, ^{159}Tb, ^{163}Dy, ^{165}Ho, ^{166}Er, ^{169}Tm, ^{172}Yb, ^{175}Lu, ^{178}Hf and ^{181}Ta. Concentrations were calculated using Iolite v.4.5 (Paton et al., 2010, 2011) with NIST610 (GeoReM database, application version 27, http://georem.mpch-mainz.gwdg.de; Jochum et al., 2005) as the primary reference material and NIST612 as the secondary reference material. Calcium was the internal standard assuming stoichiometric concentrations. Measured trace element concentrations of NIST612 are typically within 5% of expected values (GeoReM database, application version 27, http://georem.mpch-mainz.gwdg.de; Jochum et al., 2005). All ages are presented with 2σ uncertainties and data presented in supplementary material.

3.3 In-situ mica Rb/Sr geochronology

All analyses for Rb/Sr geochronology were performed in-situ in polished thin sections at the ALIPP6 lab (ISTeP, Sorbonne University, Paris) using an Excimer 193 nm Analyte G2 Teledyne laser ablation system coupled with an Agilent 8900 triple-quadrupole ICP-MS/MS coupled with a reaction cell ORS[4]. The acquisition protocol is modified from Zack and Hogmalm (2016) and Hogmalm et al. (2017), using N_2O as the reaction gas, to analyze relatively low Sr and Rb concentrations in metamorphic mica. Analyses were performed in thin sections to preserve textural relationships with 50 µm spots with a repetition rate of 8 Hz and applying a fluence of ca. 4.46 J/cm^2 across 16 seconds of ablation. The analytical setup was optimized for maximum sensitivity in gas mode for the targeted mass isotopes in the reference material NIST610 (m/z set for the first and second quadrupoles respectively at: 85 and 85; 86 and 102 then 88 and 104). Isotopic ratio from mica were normalized to repeated analyses of the USGS reference material BCR-2G (Elburg et al., 2005) with ATHO-G (Jochum et al., 2011) and BHVO-2G (Elburg et al., 2005) used as secondary USGS reference materials to assess data quality.

We routinely measured a range of major and trace elements (Na, Mg, Al, Si, K, Ti, Fe during 0.1 ms and Nb, Ba, Cs during 2 ms) together with Rb and Sr isotopes (during 0.1 s) to gain information on chemical variations of analyzed phases as well as detecting (and excluding) signals from inclusions and/or alteration zones. Concentrations were calculated per formula unit considering 1 p.f.u. for K and using BCR-2G as the primary reference material (GeoReM database, application version 27, http://georem.mpch-mainz.gwdg.de; Jochum et al., 2005). Analyzed isotopic ratios of the secondary reference material are within 5% uncertainty of the accepted value. Data reduction and instrument drift correction is realized with a homemade Matlab program and isochron age calculation is achieved with the IsoplotR software (Vermeesch, 2018). Data overdispersion is corrected by additional uncertainty based on repeated analyses on reference material ATHO-G. All ages are presented with 2σ uncertainties, see supplementary material for further details.

3.4 Thermodynamic modelling

Thermodynamic modelling was performed for four samples in the NCKFMASHTO system using the Perple-X software (version 6.8.4; Connolly 1990, 2005). Their chemical composition was estimated by averaging of thin-section surface quantitative composition scans using a FEG-SEM and are as follow in oxide mass percentage: JA26 (SiO_2 49.74, TiO_2 1.00, Al_2O_3 30.87, FeO 10.00, Fe_2O_3 1.77, Mn 0.00, MgO 1.18, CaO 0.32, Na_2O 0.83 and K_2O 3.82); SK1915g (SiO_2 74.50, TiO_2 0.86, Al_2O_3 13.99, FeO 5.05, Fe_2O_3 0.89, Mn 0.07, MgO 1.19, CaO 0.24, Na_2O 0.81 and K_2O 2.30); PB1828a (SiO_2 57.13, TiO_2 1.08, Al_2O_3 21.57, FeO 8.08, Fe_2O_3 0.00, Mn 0.29, MgO 1.84, CaO 0.45, Na_2O 0.53 and K_2O 4.75) and BS1824C (SiO_2 61.30, TiO_2 0.87, Al_2O_3 22.36, FeO 7.13, Fe_2O_3 0.00, Mn 0.12, MgO 2.56, CaO 0.58, Na_2O 0.56 and K_2O 4.13). Garnets in sample PB1828a display well-defined zoning with distinct cores that were substracted from the surface composition to calculate the bulk composition relevant to infer peak equilibrium conditions. The thermodynamic dataset from Holland and Powell (2011) was used with the following set of activity models for solid solutions: melt, chlorite, biotite, orthopyroxene, garnet, white mica, chloritoid (White et al., 2014), ilmenite (White et al., 2000), epidote (Holland and Powell, 2011) and feldspar (Holland and Powell, 2003). Pseudosection calculation was performed with excess water owing to the abundance of hydrated phases. In the absence of carbonates and negligible presence of organic matter in the studied sample, CO_2 was neglected and a fixed water activity of 1 was used for the fluid. The influence of the redox state was investigated by testing Fe^{3+}/Fe_{TOT} mass ratios of 0, 0.15 and 0.25 following White et al. (2014) and Ague (1991), and using the best fit to relative volume proportions.

4 Results

4.1 Petrography and mineral chemistry

The samples from six different metamorphic complexes, including five from the Kashmar-Kerman Tectonic Zone, were studied and dated in order to constrain their P-T-t evolution. Our main focus was on the Eastern domain of the KKTZ (Sarkuh, Tashk and Boneh-Shurow complexes), where the metamorphism, which is poorly characterized, is considered Paleozoic based on one U-Pb zircon age (Ramezani and Tucker, 2003). Only limited structural data exist for these tectonometamorphic units (Ramezani and Tucker, 2003; Verdel et al., 2007; Masoodi et al., 2013; Soleimani et al., 2021), such that their internal deformation and the relationships between them is still poorly understood, particularly for the Sarkuh complex. In the Central domain, four samples were studied in the Posht-e-Badam complex, whose timing of metamorphism is constrained by one Ar-Ar amphibole age (Kargaranbafghi et al., 2012). In the Western domain, two samples were dated for further validation of our method since radiometric and petrological data for the Chapedony complex are tightly constrained (Ramezani and Tucker, 2003; Verdel et al., 2007; Kargaranbafghi et al., 2012, 2015). Since the Jandaq complex is not only related to the subducted Anarak complex (Zanchi et al., 2009b; Bagheri and Stampfli, 2008) but also shows a HT-MP metamorphism similar to that of the KKTZ (Ramezani and Tucker, 2003; Bagheri and Stampfli, 2008), several samples were dated and their metamorphic peak was estimated.

4.1.1 Sarkuh complex

Sampling in the Sarkuh complex, which exposes large-scale folds outlined by carbonate horizons (Fig. 5a), was focused on the micaschists and mafic amphibolites. Mineral occurrences and the composition of garnet, phengite, biotite and staurolite are presented in Table 2. The following abbreviations are hereafter used to describe mineral chemistry (Fig. 6): X_{Mg}=Mg/(Mg+Fe_{TOT}); X_{Na}=Na/(Na+Ca+K) and X_K=K/(Na+Ca+K).

Eleven micaschist samples (Table 2) contain garnet in a matrix of biotite, white mica, quartz and plagioclase with minor oxide. Four of them contain large pluri-millimetric grains of staurolite either rich in quartz inclusions (Fig. 5b; SK1908b and SK1911) or with conspicuous hourglass zoning (though not related to major element zoning) and garnet inclusions, in an organic matter-rich matrix (SK1808 and SK1912b; Fig. 5c). Five samples contain aluminosilicates with minor tourmaline (Fig. 5d; X_{Mg}=0.60-0.64; X_{Na}=0.83-0.85; samples SK1806b, SK1809 and SK1814). Sample SK1806b contains fibrous and prismatic sillimanite with minor K-feldspar, tourmaline and apatite. Sample SK1809 contains centimeter-large grains of andalusite, with staurolite and biotite inclusions and partly replaced by biotite and sillimanite (Fig. 5e). Sample SK1814 (Fig. 5d) contains kyanite partly replaced by both fibrous and prismatic sillimanite, white mica and biotite. Sample SK1915g contains kyanite relicts partly pseudomorphed by biotite and sillimanite. Sample SK1923 shows cm-scale andalusite crystals pseudomorphed by biotite, white mica, quartz and sillimanite. It also contains rounded pluri-millimetric K-feldspar grains with quartz and biotite inclusions. Some samples neither contain staurolite nor aluminosilicates (SK1812a and SK1919).

Two samples are mainly composed of quartz, plagioclase and biotite with minor garnet partly retrogressed by chlorite (X_{Mg} = 0.55-0.58; SK1903b and X_{Mg} = 0.27-0.65; SK1910) and with minor apatite. Sample SK1916b is a vein with large centimeter-scale grains of tourmaline (X_{Mg} = 0.44-0.54; X_{Na} = 0.79-0.88) and white mica, within a matrix of quartz, plagioclase and minor biotite. Garnet is found both in the matrix and as inclusion in tourmaline. Sample SK1806a is an undeformed amphibolite-facies volcanoclastic rock with amphibole (X_{Mg} = 0.56-0.55; X_{Na} = 0.21-0.22; X_K = 0.04-0.05), plagioclase, quartz, oxide and partly retrogressed biotite. Sample SK1913a is a deformed amphibolite with garnet, amphibole (X_{Mg} = 0.42-0.49; X_{Na} = 0.11-0.15; X_K = 0.07-0.10), plagioclase, quartz, biotite (X_{Mg} = 0.48-0.51; Ti pfu = 0.12-0.21) and oxide. Retrogression is shown by the presence of garnet partly replaced by a complex mixture of biotite (X_{Mg}=0.45-0.55; Ti pfu=0.06-0.18), chlorite (X_{Mg} = 0.42-0.54), epidote (Fe^{3+} pfu = 0.29-0.45), pumpellyite (X_{Mg} = 0.37-0.70) and apatite (Fig. 5f).

4.1.2 Boneh-Shurow complex

The northern area of the Boneh-Shurow complex mainly consists of highly deformed gneisses showing migmatitic textures (Fig. 7a) and abundant K-feldspar forming porphyroblasts or distinct layers (Fig. 7b,c). Our four samples (BS1837, BS1947, BS1952e, BS1952g) are foliated gneisses with alternating quartz-plagioclase-K-feldspar layers and amphibole (X_{Mg} = 0.16-0.49; X_{Na} = 0.09-0.27; X_K = 0.04-0.20)-epidote (Fe^{3+} pfu = 0.36-0.68)-garnet layers. Pluri-millimetric titanite grains are present in both the matrix and as inclusion in garnet (Fig. 7d, e). In sample BS1947, amphibole and biotite overgrowths, with minor chlorite, are found around the preexisting minerals and in garnet fractures. In sample BS1952e, biotite is present in amphibole fractures. In sample BS1952g, garnet and plagioclase host a few large biotite inclusions (~200 µm), as well as some retrograde chlorite.

The central (BS1824C, BS1924, BS1925, BS1930) and southern (BS1817d, BS1931, BS1933B) areas of the Boneh-Shurow complex mostly comprise micaschists showing either the transition from andalusite to sillimanite (BS1925), kyanite to sillimanite (BS1824C), or andalusite to kyanite (Fig. 7h) in a biotite + white mica + quartz + plagioclase matrix with minor oxide. Mafic amphibolite boudins are also present (BS1930). Sample BS1824C is a micaschist with garnet, K-feldspar, prismatic sillimanite and kyanite relics showing transformation to sillimanite. Garnet grains are highly deformed yet preserve an helicitic texture with kyanite and/or sillimanite inclusions (Fig. 7f, g). K-feldspar is present as large pluri-millimetric rounded grains with biotite and quartz inclusions, and shows evidence of albite exsolution (Fig. 7i). Sample BS1924 is a garnet-, K-feldspar and kyanite-bearing micaschist where K-feldspar is again pluri-millimetric and shows rounded grains with biotite and quartz inclusions. Garnet grains are deformed with asymmetric pressure shadows and contain biotite inclusions (X_{Mg} = 0.21-0.47; Ti pfu = 0.090.23). Biotite is partly retrograde and replaces garnet and kyanite. A few tourmaline grains (X_{Mg} = 0.60-0.64; X_{Na} = 0.84) are present. Sample BS1925 is a garnet micaschist with large centimeter-scale rounded grain of andalusite transforming to sillimanite with white mica pressure shadows. Sample BS1931 is a garnet micaschist with pluri-millimetric white mica. Sample BS1933b contains minor garnet and white mica in a biotite-rich matrix. Sample BS1930 is an undeformed amphibolite with garnet, amphibole (X_{Mg} = 0.34-0.40; X_{Na} = 0.19-0.23; X_K = 0.06-0.08), plagioclase, quartz and retrograde biotite. Titanite is present in the matrix and in the garnet rims. Sample BS1817d is a deformed amphibolite with garnet, amphibole (X_{Mg} =0.41-0.45; X_{Na} = 0.25-0.29; X_K = 0.02-0.03), partly retrogressed biotite, plagioclase, quartz, minor oxide and retrograde chlorite (X_{Mg} = 0.42-0.59).

4.1.3 Tashk complex

Sample TK1802a is a garnet micaschist with an organic matter-rich matrix made of white mica, plagioclase, quartz and oxide. Intergrown biotite and chlorite (X_{Mg} = 0.46-0.52) are found in garnet pressure shadows. Sample TK1802c is a deformed amphibolite with amphibole (X_{Mg} = 0.53-0.61; X_{Na} = 0.24-0.26; X_K=0.05-0.07), plagioclase, quartz and biotite. Abundant titanite overgrowths are found around ilmenite (Fig. 8a). Sample TK1802b is an undeformed metacarbonate with large centimeter-scale, probably inherited, lozenge-shape K-feldspar porphyroblasts, phlogopite, as well as minor oxide and titanite (Fig. 8b).

4.1.4 Posht-e-Badam complex

Sample PB1828a, PB1828b and PB1936c are micaschists with pluri-millimetric garnet grains overgrown by staurolite within a matrix of white mica, biotite, sillimanite, quartz and plagioclase with minor oxide and kyanite relics. Sillimanite has co-crystalized with white mica and biotite in apparent equilibrium with the garnet rim (Fig. 8e). Staurolite growth postdates that of sillimanite and of the garnet rim (Fig. 8d). Sample PB1938 is a micaschist with altered garnet and staurolite, within a matrix of white mica, quartz, plagioclase and minor oxide. This sample is partly foliated, with a biotite rich layer containing white mica, staurolite and a few tourmaline grains (X_{Mg} = 0.45-0.57; X_{Na} = 0.61-0.84) which appear to postdate the formation of white mica (Fig. 8f).

4.1.5 Chapedony complex

Samples CH1823 is a foliated gneiss with alternating layers made of quartz and plagioclase (X_{Na} = 0.66-0.78; X_K = 0.01-0.03) and layers hosting rounded grains of K-feldspar with biotite inclusions (X_{Mg} = 0.49-0.55; Ti pfu = 0.15-0.19) within a quartz and biotite matrix (X_{Mg} = 0.42-0.55; Ti pfu = 0.05-0.14) with minor tourmaline (X_{Mg} = 0.70-0.72; X_{Na} = 0.70-0.75). Sample CH1842 is a quartz-plagioclase-biotite micaschist.

4.1.6 Jandaq complex

Sample JA17b is a micaschist with centimeter-scale, altered garnet partly replaced by biotite and chlorite (X_{Mg} = 0.33-0.40) and staurolite porphyroblasts within a matrix of quartz, plagioclase and white mica. Sample JA26 is a quartz-rich micaschist with co-crystalized chloritoid (X_{Mg} = 0.11-0.12) and white mica, with minor plagioclase, epidote and oxide (Fig. 8c). Sample JA28b is a garnet micaschist with minor staurolite in a matrix composed of quartz, plagioclase, white mica, with partly retrograde biotite, chlorite and oxide.

4.2 Thermobarometry

We applied the amphibole-plagioclase thermobarometer of Holland and Blundy (1994) and Molina et al. (2015). Results with standard deviation are 696 ± 30°C and 10.5 ± 1.8 kbar (SK1913a) and 760 ± 24°C and 8.5 ± 0.5 kbar (SK1806) for the Sarkuh complex; 641 ± 9°C and 7.3 ± 0.6 kbar (BS1952g) and 646 ± 12°C and 7.7 ± 1.2 kbar (BS1930) for the Boneh-Shurow complex; 655 ± 14°C and 4.3 ± 0.7 kbar (TK1802c) for the Tashk complex.

The formation temperature of dated titanite is estimated with the Zr content using the thermobarometer of Hayden et al. (2008). In samples BS1837, BS1952e and BS1947, the activity of SiO_2 is considered as 1 because of the presence of quartz and the activity of TiO_2 is considered between 0.5 and 1 because of the absence of rutile (Hayden et al., 2008). By varying the activity of TiO_2 and the pressure between 6.5 and 9.5 kbar, we obtain a similar range of formation temperature in samples BS1837 (674-768°C), BS1952e (664-769°C) and BS1947 (667-789°C). For sample BS1930 and TK1802c, the formation temperature is poorly constrained because of the presence of impurities and the absence of quartz leading to an activity of SiO_2 between 0.5 and 1 (Hayden et al., 2008). The temperature range is 618-823°C for BS1930 (with pressure between 6.5 and 9.5 kbar) and 602-886°C for TK1802c (with pressure between 3.5 and 5 kbar).

Thermodynamic modelling was conducted on HT-MP samples from the Sarkuh (SK1915g), Boneh-Shurow (BS1824C) and Posht-e-Badam complexes (PB1828a). The estimated peak P-T area is defined by the Grt-Sil-Bt-Ph-Qz paragenesis (Figs. 8e, 9b, c) and by the composition of biotite in equilibrium with sillimanite. The whole-rock composition of sample PB1828a (Posht-e-Badam), where garnets are centimeter-scale and abundant (10-15%), was corrected by subtracting the mean composition of prograde garnet cores, which may no longer have been part of the rock chemical system at peak conditions. This appeared unnecessary for the other samples, since modal proportions of garnet in SK1915g and BS1824c are low (<5%) and since it shows no preserved prograde zoning. Removal of garnet cores also has a negligible impact on biotite composition. Thermodynamic modelling was also conducted for the Jandaq complex (sample JA26; Fig. 9d). In the four pseudosections, the predicted Ti-bearing phase (rutile for BS1824C, JA26, PB1828a and ilmenite for SK1915g) and mineral modal compositions correspond to the thin section observations.

The pseudosection for the Sarkuh complex yields P-T conditions around 6.5-8.5 kbar and 685-755°C, based on the X_{Mg} (0.32-0.39) and Ti content (0.11-0.22 pfu) of biotite, in the range of potential melting. In the estimated P-T area, garnet composition (Alm_{79-74} Sps_{2-10} Grs_{2-6}) matches that of microprobe data (Alm_{80-83} Sps_{7-5} Grs_{1-2}). Predicted modal (volume percent) abundances, i.e. 1-5% garnet, 8-15% biotite, 8-10% sillimanite and 5-15% white mica, are in agreement with observations. The pseudosection for the Posht-e-Badam complex gives P-T conditions around 6.5-7.5 kbar and 650-695°C, based on the X_{Mg} (0.41-0.48) and Ti content (0.09-0.13 pfu) of biotite. Predicted modal abundances are ~6% garnet, ~17% biotite, ~8% sillimanite and ~35% white mica. Garnet gives a composition (Alm_{74-75} Sps_{4-6} $Grs_{4.5-5}$) again similar to that of microprobe data (Alm_{65-81} Sps_{23-5} Grs_{4-6}). Ilmenite postdates rutile, although both crystals can be observed together in some areas. The pseudosection for the Boneh-Shurow complex gives P-T conditions around 7.5-9.5 kbar and 700-790°C, based on the X_{Mg} (0.43-0.56) and Ti content (0.15-0.24 pfu) of biotite. This paragenesis likely formed past the solidus (8-9.5kbar and 750-790°C) to explain the abundance of K-feldspar (i.e. melt in the pseudosection, Fig. 7i). Predicted modal abundances are 5-10% garnet, 15-25% biotite, 10-15% sillimanite and 15-25% white mica. Garnet gives a composition (Alm_{68-74} $Sps_{2-4.5}$ Grs_{5-8}) similar to that of microprobe data (Alm_{72-78} Sps_{16-5} Grs_{2-3}) but with a higher grossular content. The pseudosection for the Jandaq complex gives P-T conditions around 11.6-13 kbar and 410-480°C, based on the X_{Mg} of chloritoid (0.10-0.12) and the Si content of coexisting white mica (3.08-3.12 pfu), and on the presence of paragonite, epidote, ilmenite, rutile and chlorite (Fig. 9d, 8c). The P-T estimated area predicts realistic mineral abundances for white mica (37-39%) and chloritoid (28-30%).

In order to further assess the retrograde P-T path, thermobarometric calculations were performed on sample PB1828a using Thermocalc V. 3.21 (Holland and Powell, 1998, Holland and Powell, 2011). The H_2O activity was set to 1 based on the lack of significant halogen and carbon contents in hydrous minerals. Mineral activities were determined using the AX software (Holland and Powell, 1998; updated in 2011). The retrograde assemblage of staurolite ($Mg_{0.534}\,Fe^{2+}_{2.921}\,Al_{18.232}\,Si_{7.459}\,O_{44}\,(OH)_4$), white mica ($K_{0.866}\,Na_{0.172}\,Al_{2.932}\,Mg_{0.045}\,Fe^{2+}_{0.065}\,Si_{2.970}\,O_{10}\,(OH)_2$), biotite ($K_{0.902}\,Na_{0.037}\,Al_{1.777}\,Mg_{1.114}\,Fe^{2+}_{1.253}\,Si_{2.639}\,Ti_{0.107}\,O_{10}\,(OH)_2$), plagioclase ($K_{0.003}\,Na_{0.607}\,Ca_{0.423}\,Al_{1.478}\,Si_{2.523}\,O_8$) and garnet rim ($Ca_{0.215}\,Mn_{0.105}\,Mg_{0.292}\,Fe^{2+}_{2.269}\,Fe^{3+}_{0.179}\,Al_{2.037}\,Si_{2.894}\,O_{12}$) gives a P-T estimate with standard deviation of 629 ± 27 °C and 6.5 ± 1.1 kbar and a sigfit of 0.97. This estimate is close to the estimated peak condition (6.5-7.5kbar and 650-695°C) and coincides, in the pseudosection, with the destabilization of sillimanite to staurolite (Fig. 9) at the beginning of the retrograde path.

We also applied the methods of Henry et al. (2005) and Wu and Chen (2015), with the latter taking pressure into account, to estimate temperature based on peak biotite composition (Tab. 3). Results show some discrepancy between the Wu and Chen (2015) method (using pressure estimation of the pseudosections) and the Henry et al. (2005) method: 650 ± 16°C at 10.5 kbar versus 544 ± 22°C (sample SK1913a); 522 ± 25°C at 4.3 kbar versus 525 ± 33°C (TK1802c); 594 ± 16°C at 7 kbar versus 404 ± 38°C (PB1828a); 692 ± 26°C at 9 kbar versus 538 ± 31°C (BS1824C). Using the pressure calculated from the pseudosection, the revised method of Wu and Chen (2015) for the Ti in biotite give higher formation temperatures, consistent with our other temperature estimates. The method of Henry et al., 2005 is used to index all biotite dates without a pressure estimation.

4.3 Titanite U/Pb geochronology

We dated three gneisses from the northern Boneh-Shurow complex. All give similar lower intercept dates (Fig. 10): 178.0 ± 1.2 Ma (BS1952e); 179.6 ± 1.0 Ma (BS1947) and 187.4 ± 0.9 Ma inclusions and those from the matrix. However, titanite from BS1837 is mostly in garnet core, which could explain a partly prograde older date. Another sample from the central part Boneh-Shurow complex gives a less well-constrained date: BS1930 (191.3 ± 4.0 Ma), due, in part, to smaller titanite that contain significant impurities, and have lower radiogenic/common Pb ratios. This date, nevertheless, overlaps with that obtained for BS1837 in the northern part.

One sample from the Tashk complex (TK1802c; Fig. 10), with titanite filled with impurities and growing around ilmenite, yielded a poorly constrained date (225 ± 12 Ma), which while significantly different than those in the Boneh-Shurow complex, is nonetheless compatible with the Cimmerian orogeny.

4.4 Mica Rb/Sr geochronology

Results of Rb/Sr dating are presented in Table 3 and Figure 11 for biotite, and in supplementary data for white mica. The obtained Rb/Sr dates may represent crystallization or cooling ages, and are therefore compared to the Si content of white mica and to the Ti-in-biotite temperature estimated using the thermometer of Henry et al. (2005). Commonly reported closure temperatures for the Rb–Sr geochronometer range from 500°C to >600°C for white mica (e.g., Blanckenburg et al. 1989; Freeman et al. 1997; Glodny et al. 1998, 2008; Purdy and Jäger 1976) and between 300°C-450°C for biotite (Armstrong et al., 1966; Jager et al., 1967; Verschure et al., 1980; Del Moro et al., 1982; Jenkin et al., 2001).

With our Rb/Sr in-situ dating method, we obtained constrained dates for biotite with 2σ between 1.4 and 43 Ma. Constrained dates were obtained even for texturally heterogeneous or small biotite crystals, such as in sample TK1802a, where biotite is interstratified with chlorite, or sample BS1824C, where biotite appears as small inclusions in K-feldspar (Fig. 7i). In white mica, however, the spread of $^{87}Rb/^{86}Sr$ ratios is restricted, leading to poorly constrained isochron slopes and dates (2σ between 15 and 210 Ma). Using another mineral to constrain the origin of the isochron can significantly refine its slope (i.e. SK1916b with tourmaline and TK1802b with K-feldspar; Fig. 11). However, this can only be done assuming a closed system behavior and/or that minerals have co-crystalized. The date of TK1802b, in particular, must be interpreted with caution because the phlogopite and K-feldspar may have been inherited (Fig. 8b).

In the four samples from the Posht-e-Badam complex, biotite shows similar dates (158-162 Ma) and consistent Ti-in-biotite temperatures (∼353-435°C). White mica and biotite co-crystalized but two of the white mica dates are significantly older (184-270 Ma; they also have a low Si content ∼3.0 pfu).

In the northern Boneh-Shurow, biotite, mainly retrograde, gives dates ranging from 129 to 154 Ma, with similar Ti-in-biotite temperatures (∼435-485°C). In the central Boneh-Shurow, biotite, largely retrograde too, shows dates between 141 and 163 Ma, with similar Ti-in-biotite temperatures (~487-539°C; samples BS1924, BS1925 and BS1930). Biotite from sample BS1824C, whether from the matrix or as inclusion in K-feldspar, gives the same date (152-159Ma) and the same Ti-in-biotite temperature (~537-542°C). White mica dates with Si content of ~3.05-3.12 pfu overlap with biotite dates. In the southern Boneh-Shurow, retrograde biotite in BS1817d has a poorly constrained date (189 ± 25 Ma). Sample BS1933b has a biotite date (159 ± 2 Ma) and Ti-in-biotite temperature (~515°C) similar to others. Sample BS1931 gives a similar biotite date (150 ± 4 Ma) and Ti-in-biotite temperature (~424°C); its white mica date is however significantly older (234 ±22 Ma).

In the Sarkuh complex, white micas (with Si content ~3.04-3.08 pfu) generally have poorly defined dates that broadly overlap with biotite dates, save for the vein sample SK1916b, which has a significantly older white mica and tourmaline date (198 ± 15 Ma) than that of biotite (<180 Ma). Biotite in samples SK1806a, SK1812a, SK1814, SK1915g, SK1923, SK1910, SK1809 and SK1913a formed near peak and have Ti-in-biotite temperature of ~466-617°C with dates spreading from 157 to 175 Ma. Biotite in samples SK1806b, SK1919, SK1908b, SK1912b and SK1808, which is post-peak (with Ti-in-biotite temperature of ~286-549°C), shows a date spread from 149 to 177 Ma. Late retrograde biotite overgrowths in samples SK1903b and SK1911 have dates of 104 ± 23 and 122 ± 11 (with Ti-in-biotite temperatures of ~389°C and ~319°C, respectively). Metasomatic biotite from sample SK1913a is associated with chlorite, pumpellyite and apatite and has a poorly constrained date of 140 ± 43 Ma with a Ti-in-biotite temperature of ~519°C (similar to other biotite in this sample).

In samples from the Jandaq complex, white mica yields significantly older dates (468-182 Ma) than biotite (213-142 Ma), consistent with the fact that biotite formed after white mica in both samples (JA17b and JA28b). However, sample JA17b has a significantly older biotite date (202 ± 11 Ma;~360°C) than sample JA28b (148 ± 6 Ma;~390°C). White mica from sample JA26 shows a significantly higher Si content (~3.12 pfu) than in all other samples.

In samples from the Tashk complex, biotite shows a relatively large spread of date (150-182 Ma). The temperature of biotite Ti-in-biotite is similar for TK1802b and TK1802c (~460 and ~526°C respectively). The Ti content of biotite in sample TK1802a could not be measured due to interstratification with chlorite.

In the two samples from the Chapedony complex, biotite has the same date (40-44 Ma) and Ti-in-biotite temperature (~555°C).

5 Discussion

5.1 Metamorphic evolutions in Central Iran

The widespread occurrence of sillimanite or of the Grt-St-Bt paragenesis in metapelites from the Sarkuh, Boneh-Shurow and Posht-e-Badam complexes is indicative of MP-MT to MP-HT metamorphism (Tab. 2). In the Sarkuh and Boneh-Shurow complexes, some samples record the transition from andalusite to sillimanite (BS1925, SK1809, SK19323) and some from kyanite to sillimanite (BS1824c, BS1924, SK1814, SK1915g; Fig. 5). While broadly similar peak P-T conditions were obtained for both types, further work is needed to understand if these mineralogical evolutions represent somewhat different metamorphic grades and prograde paths, and therefore distinct tectonometamorphic units in these complexes.

The migmatitic texture observed in the gneisses from the northern Boneh-Shurow complex (Figs. 7a,b) supports the existence of melting. In some samples from the Sarkuh and Boneh-Shurow complexes, rounded, pluri-millimetric K-feldspar grains are found with rounded biotite and quartz inclusions and albite exsolution (samples BS1824C, BS1924, SK1806b and SK1923; Fig. 7i; Tab. 2). Biotite inclusions have similar composition and date as matrix biotite and, therefore, K-feldspar likely formed after biotite by local breakdown of white mica. The perthitic nature of the feldspar indicates it formed above albite exsolution, i.e. T>700°C (Tuttle and Bowen, 1958). These observations indicate that the Sarkuh and Boneh-Shurow complexes reached the wet solidus for metapelites, contrary to the Posht-e-Badam complex.

White mica and biotite in the Posht-e-Badam complex have respectively lower Si content (~3.03-3.18 pfu) and Ti content (~0.7-0.14 pfu) than in the Boneh-Shurow and Sarkuh complexes (Fig. 6). These compositional trends hint at lower temperature and pressure conditions for the Posht-e-Badam complex than for the Boneh-Shurow and Sarkuh complexes, and to a somewhat different P-T path. This difference is confirmed by its older metamorphic age (~219 Ma; Karagaranbafghi et al., 2012), when compared to that obtained for the Boneh-Shurow complex with titanite (~190-180 Ma; Fig. 13). In the Posht-e-Badam complex samples, staurolite is observed overgrowing garnet (Fig. 8d). Our P-T estimation for staurolite formation (629 ± 27 °C and 6.5 ± 1.1 kbar) indicates that it formed near-peak at the beginning of the retrograde path. This retrogression in the staurolite stability field is not documented in the Boneh-Shurow and Sarkuh complexes, where staurolite only appears as part of the prograde or peak paragenesis with garnet and biotite.

The pseudosections for these three complexes (Fig. 9) allow to estimate the peak P-T conditions (Grt-Sil-Bt-Ph) experienced by the Sarkuh (7-8.5 kbar, 685-755°C), Boneh-Shurow (8-9.5

kbar, 750-800°C) and Posht-e-Badam complexes (7-7.5 kbar, 670-690°C), confirming a slightly lower metamorphic peak for the latter (Fig. 14). All indicate MT- to HT-MP conditions typical of collisional gradients and are similar to the P-T estimate inferred for the Cimmerian collisional metamorphism of the Shotor-Kuh complex (Fig. 12; Rahmati-Ilkhchi et al., 2011).

In samples from the Sarkuh and Boneh-Shurow complexes, the estimated peak conditions are partly past the solidus (<30% melt, Fig. 9), as corroborated by the presence of migmatitic textures in gneisses and of rounded K-feldspar grains with albite exsolution in metapelites. However, since white mica is still preserved and no major migmatitic texture is observed in the studied metapelite samples, partial melting was probably limited (<10-20% melt). The P-T estimate for BS1824c must be taken with caution since the composition of the chemical system could have been partly modified by melting, but is nonetheless consistent with our other P-T estimates (Fig. 12).

In the Jandaq complex, the presence of both HP-LT (Ph+Cld; Fig. 8a) and MP-MT (Grt+St+Bt) paragenesis reveals the existence of two different metamorphic gradients and probably two distinct metamorphic units. We tentatively relate the first paragenesis to the Paleotethys subduction and the second one to a collisional context related to the Cimmerian orogeny. White mica from the Jandaq, Sarkuh and Boneh-Shurow complexes has similar silica contents (~3.1-3.3 pfu). Biotite from Jandaq shows a narrower range and mainly lower Ti content (~0.7-0.14 pfu) than biotite from the Boneh-Shurow and Sarkuh complexes (~0.5-0.22 pfu), confirming a higher P/T gradient for the Jandaq complex compared to the Kashmar–Kerman Tectonic Zone (KKTZ).

Thermodynamic modelling indicates peak conditions of 11.6-13 kbar, 410-480°C for the Jandaq HP-LT paragenesis, hence comparable with the HP-LT gradient of the Rasht and Anarak metamorphic complexes ascribed to the subduction of the Paleotethys (Fig. 12; Rossetti et al., 2015; Zanchetta et al., 2018). In the Tashk complex, by contrast, the absence of high pressure or high temperature diagnostic minerals indicates that it only experienced lower grade metamorphic conditions.

The peak estimates obtained from pseudosection modeling, amphibole-plagioclase and Zr in titanite thermobarometry (Holland and Blundy 1994; Hayden et al. 2008; Molina et al. 2015, Fig. 12) are mutually consistent. Estimates for the temperature of biotite formation using Henry et al. (2005) are somewhat lower (Fig. 12) and generally underestimated because pressure is not considered.

5.2 Interpretation of geochronological data

5.2.1 Interpretation of in-situ titanite, biotite and white mica dates

Calculated U/Pb titanite dates are considered here to date peak metamorphism due to the high closure temperature of titanite (~800°C; Kohn, 2017) and to the absence of significant differences in age or composition between matrix titanite and titanite inclusions in garnet.

Calculated Rb/Sr dates are considered to mark the time when diffusion of Sr in the crystalline network and across mineral boundaries becomes insignificant. They are therefore commonly interpreted as "cooling ages", i.e. dating cooling of the sample below the system closure temperature (Jager et al., 1967). Aside temperature, however, several parameters may influence the closure of the system, such as the cooling rate, recrystallisation, fluid-rock interactions, grain size and interaction with adjacent minerals. Some authors have estimated that fluid- and deformation-enhanced recrystallisation is more efficient than diffusive re-equilibration (Villa, 2010).

In the studied samples, biotite formed at peak or near peak conditions, at temperatures significantly higher than its assumed typical closure temperature (300-450°C). Therefore, the Rb/Sr dates for biotite most likely reflect cooling ages (or later resetting through fluid infiltration or recrystallization). The potential higher closure temperature of white mica (500°C to >600°C) makes the interpretation of Rb/Sr for this mineral more ambiguous: they could correspond to either crystallization or cooling ages. Dates obtained for white mica in this study are rather poorly constrained because of relatively low Sr ratios (Fig. 11), which is best explained by the relative enrichment in Sr compared to Rb in white mica (Bebout et al., 2007). In high grade rocks, the coexistence of white mica and biotite induces a partitioning of Sr and Rb with Sr favoring white mica (Yang and Rivers, 2000). The in-situ Rb/Sr technique applied here therefore provides optimal constraints, through biotite, on the cooling history of metamorphic rocks, but is not conveniently suited to constrain the peak or early cooling stages.

5.2.2 An exhumation history punctuated by Cimmerian events?

Almost all Rb/Sr ages are Jurassic and fit in the range of the Mid- (∼170 Ma) to Late (∼140 Ma) Cimmerian tectonic events (Fürsich et al., 2009b; Wilmsen et al., 2015; Fig. 13; Tab. 3), with three main populations of biotite cooling ages:

(i) ∼170 Ma, for the Tashk and Sarkuh complexes.

(ii) ~160-150 Ma for the Boneh-Shurow and Posht-e-Badam complexes, with a narrow age range for the latter. In the Boneh-Shurow complex, ages tend to decrease from 160 to 140 with decreasing formation temperatures for biotite (Fig. 13), with the exception of one age in the southern part. This may reflect gradual exhumation associated with biotite formation. No such trend is observed in the Sarkuh complex, whose ages range mainly between 170 and 150 Ma.

(iii) A subordinate population ranging between 150 and 140 Ma at Jandaq, Sarkuh and Boneh-Shurow complexes. Some biotite ages between 140 and 100 Ma, in the Sarkuh complex, stand out as significantly younger and may be related to reequilibration during final exhumation.

Some older Rb/Sr ages are also obtained (Fig. 13). Two white mica ages in the Posht-e-Badam complex (228 ± 42 and 214 ± 30 Ma), and one from the Boneh-Shurow complex (234 ± 22 Ma), are significantly older than the biotite ages obtained for the same samples, and are synchronous with the Eo-Cimmerian event. The biotite Rb/Sr ages of this study are consistent with previously published cooling ages for the Posht-e-Badam, Boneh-Shurow and Jandaq complexes (Fig. 13, Tab. 2) and are altogether similar. They are also internally consistent with this study titanite ages (177-237 Ma; Figs. 10,13). These ages stand in contradiction with previous suggestions of an early Paleozoic metamorphism for the Sarkuh, Tashk and Boneh-Shurow complexes, which were based on a single U-Pb Zircon age of 547.6 ± 2 Ma (Ramezani and Tucker, 2003). Our results instead support the Cimmerian Ar-Ar hornblende age obtained for one sample of the Posht-e-Badam complex (219.2 ± 1.2 Ma; Karagaranbafghi et al., 2012). In the Jandaq complex, apart from one poorly constrained Carboniferous Rb/Sr age, other Rb/Sr ages lie between 180 and 260 Ma, which would either coincide with the Cimmerian orogeny or a late stage of Paleotethyan subduction (Tab. 3, Figs. 12, 13). Given that the P-T conditions experienced by this sample (JA26) align on the same HP-LT gradient as the subducted Anarak or Rasht complexes (Fig. 12), this age more likely relates to a subduction stage, possibly partial reset during the Cimmerian orogeny.

In the Tashk complex, the presence of inherited biotite and K-feldspar could explain the older titanite age obtained for the TK1802b sample. The other biotite ages (168 ± 3 and 153 ± 3 Ma) are in the range of biotite ages of the neighboring Sarkuh complex. Verdel et al (2007), however, obtained older Ar-Ar biotite ages between 218 and 295 Ma. Furthermore, the onlap of Permian and Triassic shallow-marine carbonates onto the Tashk complex demonstrate its exposure before the onset of the Cimmerian orogeny. Considering our U-Pb titanite age (225 ± 12 Ma) and P-T estimate (655 ± 15°C; 4-5 kbar; Fig. 12), these observations collectively indicate shallow burial and heating of the Tashk complex during the Cimmerian Orogeny and its subsequent exhumation after the Mid-Cimmerian event. Further investigation of the tectonic relationships between the Tashk complex and the adjacent higher-grade complexes of the Boneh-Shurow and Sarkuh complexes is needed to explain the detailed stacking of the various tectonometamorphic units. At the other end of the spectrum, the two biotite ages obtained for the Chapedony massif (42.5 ± 2.0 and 42.7 ± 1.8 Ma) confirm its cooling and exhumation as a core-complex during the Eocene (Kargaranbafghi et al. 2015).

As discussed above (section 5.2.1), biotite ages are interpreted to reflect cooling of the metamorphic terranes below 300-450°C during the Jurassic and the Cretaceous. During the Jurassic, the Yazd block and the KKTZ were exposed (Figs. 3,14), whereas the Tabas and Lut Blocks formed a submerged extensional basin with large tilted fault blocks (Figs. 3,14; Wilmsen et al. 2009b; Salehi et al. 2018). Provenance studies of the Lower Jurassic Tabas sedimentary record point to a dominant recycled-orogen source, possibly from the KKTZ (Salehi et al., 2018). This indicates significant erosion of the KKTZ during the lower Jurassic and before the Mid-Cimmerian event. After the Mid-Cimmerian event, Upper Jurassic sedimentation shows increased subsidence and development of a carbonate platform in the Tabas Block (Wilmsen et al., 2009a), similar to what is observed in the Alborz (Fürsich et al., 2009b). This may be indicative of a prolonged extensional setting responsible for the exhumation of the Sarkuh and Boneh-Shurow complexes. This would be consistent with claims of core-complex formation along the KKTZ at ~165 Ma (Masoodi et al., 2013; Soleimani et al., 2021). However, while the Sarkuh and Boneh-Shurow complexes were interpreted as sharing the same deformation and exhumation history (Masoodi et al., 2013), the 10 Myr difference of biotite cooling ages (Fig. 13) points to somewhat diachronous exhumation for the two sectors.

Given that the biotite ages obtained here are mostly younger than 170 Ma, we propose that cooling and exhumation started and/or accelerated during the Mid-Cimmerian event, probably as a result of renewed extension. No compressive event is indeed observed in the KKTZ at 170 Ma, nor any magmatic stage which may have reset ages through heating. The data also mark a diachronous exhumation of the different complexes of the KKTZ, with earlier exhumation in the east than in the west. This may relate to the large-scale fault bounding the KKTZ to the east, which accommodated the Jurassic rotation of the Tabas block (Wilmsen et al., 2009a; Fig. 3).

5.3 Geodynamic implications

We report the existence of a collisional MP-HT metamorphic imprint in the KKTZ, in the Boneh-Shurow, Sarkuh and Posht-e-Badam complexes, with peak burial to depths of 20-25 km at 180-190 Ma for the Boneh Shurow complex and possibly somewhat earlier, during the Eo-Cimmerian event, for the Posht-e-Badam complex (Fig. 12; ~210 Ma; Karagaranbafghi et al. 2012). Shortening accompanied the tectonic stacking of these units, as shown by the juxtaposition of the Sarkuh complex onto the lower pressure Tashk complex (Fig. 4). Rb/Sr geochronology reveal a main cooling and exhumation stage ~170-160 Ma for all units, hence during or immediately postdating Mid-Cimmerian times.

Their exhumation likely took place through extensional tectonics accompanied by the formation of core-complexes (Masoodi et al., 2013; Soleimani et al., 2021). On a broader scale, the exhumation of the Boneh-Shurow, Sarkuh, Posht-e-Badam and Tashk complexes coincided with distributed crustal-scale extension in Iran (Fig. 14, Fürsich et al. 2009b; Wilmsen et al. 2009b,a), marked by pronounced subsidence, normal faulting and block rotation in the Tabas block (Wilmsen et al., 2009b; Salehi et al., 2018) and by the onset of seafloor spreading in the South Caspian Basin (Fürsich et al., 2009b). Meanwhile, widespread and profuse arc magmatism related to the subduction of the Neotethys is recorded in the transtensional Sanandaj-Sirjan zone (Agard et al., 2011; Hassanzadeh and Wernicke, 2016), as well as arc-related magmatic activity and HT-LP metamorphism in the Deh-Salm and Anjul metamorphic complexes to the north of the Lut block (Bröcker et al., 2016). During the Middle Jurassic, before the anticlockwise rotation of the CEIM (Mattei et al., 2015), the Lut block was located, like the Sanandaj-Sirjan Cimmerian block, in the upper plate magmatic arc setting of the Neotethyan subduction zone (Figs. 3, 14; Esmaeily et al. 2005; Bröcker et al. 2014; Mahmoudi et al. 2010). This period between 170 and 160 Ma therefore corresponds to an important geodynamic evolution, from Paleotethys closure and Eo-Cimmerian orogeny to a prevalence of Neotethys subduction dynamics with back-arc basin formation from the Middle Jurassic onwards (Agard et al., 2011; Moghadam and Stern, 2015). We propose that the prevalence of cooling ages between 170 and 160 Ma reflects an increase of exhumation rates in the KKTZ during that period.

In contrast, the origin of the collisional metamorphism documented here is enigmatic: while peak burial appears broadly coeval with the Eo-Cimmerian orogeny associated with Paleotethys closure (220-185 Ma; Wilmsen et al., 2009b), the KKTZ is located several hundred kilometers away from the suture zone, with no evidence for significant shortening and thickening in between. A similar collisional MP-HT metamorphism of Cimmerian age is observed in three distinct areas (KKTZ, Jandaq and Shotor Kuh; Rahmati-Ilkhchi et al., 2010, 2011) located along large-scale strike-slip systems, which were active throughout the Mesozoic (Figs. 1, 2; KKTZ fault system: Masoodi et al. 2013; Doruneh fault: Berra et al. 2017; Malekpour-Alamdari et al. 2017; Naini-Kalmard fault: Wilmsen et al. 2021). Formation and exposure of these different complexes may therefore tentatively be related to the accommodation of transcurrent deformation following Paleotethys closure and subsequent exhumation. There is no petrological or radiochronological evidence to support that this metamorphism might have occurred earlier (e.g., during the Panafrican or Paleozoic) and been overprinted during the Cimmerian event.

The KKTZ and the Yazd block were mainly emergent during the Jurassic period with no significant sedimentary burial throughout the Jurassic (Dercourt et al. 1986; Fürsich et al. 2003;

Wilmsen et al. 2003, 2005, 2010). Additionally, Cimmerian deformation and metamorphism appear absent from the Yazd block: the Triassic rocks are weakly deformed (Salehi et al., 2018) and the molasse-type sediments marking the closure of the Paleotethys are metamorphosed in the greenschist facies at most (i.e., the Shemshak formation; Zanchi et al., 2015). The observed collisional metamorphism appears restricted to the KKTZ and did not significantly affect the rest of the CEIM.

Two possible tectonic settings can therefore be envisioned for the genesis of this collisional metamorphism: (i) crustal shortening and burial occurred as a result of the main collisional movements, in the vicinity of the Paleotethys suture zone, and the metamorphosed units were later displaced and offset along large-scale transcurrent faults; (ii) crustal shortening and burial took place across a weak zone/domain located outboard of the main collision zone, between the Yazd and Tabas block (I.e. to the south of the Alborz and Central Iran blocks; Fig. 3, 14).

The first hypothesis implies a several hundred kilometer large displacement of the KKTZ relative to the Yazd block after the Eo-Cimmerian to reach the present-day CEIM configuration. No significant differential rotation within the CEIM is however documented by paleomagnetic data from the Triassic onwards (Soffel et al., 1996; Mattei et al., 2015). Furthermore, the Paleotethys suture zone is continuously described between Iran and Afghanistan (Fig. 1) and it is unlikely that the KKTZ was situated along the suture, east of the Yazd block in place of the Afghan block. Therefore, we favor the second hypothesis and suggest that the polyphase "Cimmerian" metamorphism and magmatism in the KKTZ (and in the Shotor Kuh area) marks the closure and shortening of rheologically weak domains, possibly small basins with thinned crust, which were still separating the Western Cimmerian blocks at the time, e.g. between the Yazd and Tabas blocks.

6 Conclusions

This study places constraints on the timing and intensity of burial and exhumation of Cimmerian metamorphic rocks in Central Iran based on combined metamorphic and geochronologic data:

(1) In-situ Rb/Sr dating of biotite yields precise and accurate cooling ages (± 2-5 Ma), mostly in the range 170-150 Ma, that are consistent between the different complexes. In contrast, white mica gives poorly constrained ages due to Sr partitioning between biotite and white mica.

(2) Results show that the central (Posht-e-Badam) and eastern (Boneh-Shurow, Sarkuh) domains of the Kashmar–Kerman Tectonic Zone (KKTZ) were buried along a Barrovian metamorphic gradient down to ~25 km (8-9 kbar; ~750°C), during the Jurassic. This stands in contradiction with former studies advocating for Paleozoic metamorphism of the eastern complexes. The higher pressure and lower temperature metamorphism of the Jandaq complex occurred earlier, during subduction of the Paleotethys.

(3) This Barrovian metamorphism is coeval with or slightly younger than the Cimmerian orogeny, as shown by titanite crystallization ages between 190 and 180 Ma. Based on paleogeographic reconstructions showing that the KKTZ lied hundreds of kilometers south of the Paleotethys suture zone, we propose that this metamorphism results from the closure and

shortening of a rheologically weak domain located outboard of the main suture, which separated the Yazd and Tabas blocks (such as a small basin with thinned crust).

(4) Exhumation of the KKTZ metamorphic rocks occurred between 170 and 140 Ma, just after the Mid-Cimmerian event (~170 Ma). This is coeval with the widespread extension documented throughout Iran, which is thought to result from upper plate extension above the Neotethyan subduction system.

Acknowledgements

This work benefited from the financial support of the bilateral cooperation program TRIGGER between France and Iran, led by the CNRS and the Geological Survey of Iran (GSI) and by the ANR EGEO Project, from the European Research Council (ERC) under the seventh Framework Programme of the European Union (ERC Advanced Grant, grant agreement No 290864, RHEOLITH). We thank the GSI, and especially the geologists and all the staff that accompanied and helped us on the field. We thank E. Delairis, O. Boudouma, M. Fialin and N. Rividi for technical and analytical support. Great thanks to many colleagues for insightful discussions, particularly M. Jentzer, C. Herviou, B. Dubacq, L. Labrousse and M. Poujol. We would like to warmly thank T. Zack for his help to set up the Rb/Sr dating and M. Button and S. Shrestha for their contributions to the titanite geochronology. We thank M. Bröcker for reviewing this manuscript, as well as I. Uysal for his comments and editorial handling.

References

Agard, P., Omrani, J., Jolivet, L., and Mouthereau, F., 2005. Convergence history across Zagros (Iran): constraints from collisional and earlier deformation. International journal of earth sciences, 94(3):401–419.

Agard, P., Omrani, J., Jolivet, L., Whitechurch, H., Vrielynck, B., Spakman, W., Monié, P., Meyer, B., and Wortel, R., 2011. Zagros orogeny: a subduction-dominated process. Geological Magazine, 148(5-6):692–725.

Ague, J. J., 1991. Evidence for major mass transfer and volume strain during regional metamorphism of pelites. Geology, 19(8):855–858.

Aistov, L., Melnikov, B., Krivyakin, B., Morozov, L., and Kiristaev, V., 1984. Geology of the Khur area (central Iran). Explanatory text of the Khur quadrangle map, 1(250.000):1–130.

Alavi, M., 1991. Sedimentary and structural characteristics of the Paleo-Tethys remnants in northeastern Iran. Geological Society of America Bulletin, 103(8):983–992.

Alavi, M., Vaziri, H., Seyed-Emami, K., and Lasemi, Y., 1997. The Triassic and associated rocks of the Nakhlak and Aghdarband areas in central and northeastern Iran as remnants of the southern Turanian active continental margin. Geological Society of America Bulletin, 109(12):1563–1575.

Anderson, J. L. and Smith, D. R., 1995. The effects of temperature and fO_2 on the Al-in-hornblende barometer. American Mineralogist, 80(5-6):549–559.

Angiolini, L., 2001. Lower and Middle Permian brachiopods from Oman and PeriGondwanan palaeogeographical reconstructions. SYSTEMATICS ASSOCIATION SPECIAL VOLUME, 63:352–362.

Angiolini, L., Balini, M., Garzanti, E., Nicora, A., Tintori, A., Crasquin, S., and Muttoni, G., 2003. Permian climatic and paleogeographic changes in Northern Gondwana: the Khuff Formation of Interior Oman. Palaeogeography, Palaeoclimatology, Palaeoecology, 191(3-4):269–300.

Armstrong, R. L., Jäger, E., and Eberhardt, P., 1966. A comparison of K-Ar and Rb/Sr ages on Alpine biotites. Earth and Planetary Science Letters, 1(1):13–19.

Bagheri, S. and Stampfli, G. M., 2008. The Anarak, Jandaq and Posht-e-Badam metamorphic complexes in central Iran: new geological data, relationships and tectonic implications. Tectonophysics, 451(1-4):123–155.

Balini, M., Nicora, A., Berra, F., Garzanti, E., Levera, M., Mattei, M., Muttoni, G., Zanchi, A., Bollati, I., Larghi, C., et al., 2009. The Triassic stratigraphic succession of Nakhlak (Central Iran), a record from an active margin. Geological Society, London, Special Publications, 312(1):287–321.

Ballato, P., Uba, C. E., Landgraf, A., Strecker, M. R., Sudo, M., Stockli, D. F., ... & Tabatabaei, S. H., 2011. Arabia-Eurasia continental collision: Insights from late Tertiary foreland-basin evolution in the Alborz Mountains, northern Iran. Bulletin, 123(1-2), 106-131.

Bebout, G. E., Bebout, A. E., and Graham, C. M., 2007. Cycling of B, Li, and LILE (K, Cs, Rb, Ba, Sr) into subduction zones: SIMS evidence from micas in high-P/T metasedimentary rocks. Chemical Geology, 239(3-4):284–304.

Berberian, M. and King, G., 1981. Towards a paleogeography and tectonic evolution of Iran. Canadian journal of earth sciences, 18(2):210–265.

Berra, F., Zanchi, A., Angiolini, L., Vachard, D., Vezzoli, G., Zanchetta, S., Bergomi, M., Javadi, H. R., and Kouhpeyma, M., 2017. The upper Palaeozoic Godar-e-Siah Complex of Jandaq: evidence and significance of a North Palaeotethyan succession in Central Iran. Journal of Asian Earth Sciences, 138:272–290.

Berra, F., Zanchi, A., Mattei, M., and Nawab, A., 2007. Late Cretaceous transgression on a Cimmerian high (Neka Valley, Eastern Alborz, Iran): A geodynamic event recorded by glauconitic sands. Sedimentary Geology, 199(3-4):189–204.

Blanckenburg, F. v., Villa, I., Baur, H., Morteani, G., and Steiger, R., 1989. Time calibration of a PT-path from the Western Tauern Window, Eastern Alps: the problem of closure temperatures. Contributions to mineralogy and Petrology, 101(1):1–11.

Boulin, J., 1991. Structures in Southwest Asia and evolution of the eastern Tethys. Tectonophysics, 196(3-4):211–268.

Bröcker, M., Rad, G. F., Abbaslu, F., and Rodionov, N., 2014. Geochronology of high-grade metamorphic rocks from the Anjul area, Lut block, eastern Iran. Journal of Asian Earth Sciences, 82:151–162.

Brown, M., 2014. The contribution of metamorphic petrology to understanding lithosphere evolution and geodynamics. Geoscience Frontiers, 5(4):553–569.

Campi, J. M., Shi, G. R., and Lehman, M. S., 2005. Guadalupian (Middle Permian) brachiopods from Sungai Toh, a Leptodus Shale locality in the Central Belt of Peninsular Malaysia Part I: Lower Horizons. Palaeontographica Abteilung A, pages 97–160.

Connolly, J., 1990. Multivariable phase diagrams; an algorithm based on generalized thermodynamics. American Journal of Science, 290(6):666–718.

Connolly, J. A., 2005. Computation of phase equilibria by linear programming: a tool for geodynamic modeling and its application to subduction zone decarbonation. Earth and Planetary Science Letters, 236(1-2):524–541.

Davoudian, A. R., Genser, J., Neubauer, F., & Shabanian, N., 2016. ^{40}Ar/^{39}Ar mineral ages of eclogites from North Shahrekord in the Sanandaj–Sirjan Zone, Iran: implications for the tectonic evolution of Zagros orogen. Gondwana Research, 37, 216-240.

Davoudzadeh, M. and Weber-Diefenbach, K., 1987. Contribution to the paleogeography, stratigraphy and tectonics of the Upper Paleozoic of Iran. Neues Jahrbuch für Geologie und Paläontologie. Abhandlungen, 175(2):121–146.

Del Moro, A., Puxeddu, M., Di Brozolo, F. R., and Villa, I., 1982. Rb/Sr and K-Ar ages on minerals at temperatures of 300–400 C from deep wells in the Larderello geothermal field (Italy). Contributions to Mineralogy and Petrology, 81(4):340–349.

Dercourt, J., Zonenshain, L., Ricou, L.-E., Kazmin, V., Le Pichon, X., Knipper, A., Grandjacquet, C., Sbortshikov, I., Geyssant, J., Lepvrier, C., et al., 1986. Geological evolution of the Tethys belt from the Atlantic to the Pamirs since the Lias. Tectonophysics, 123(14):241–315.

Domeier, M. and Torsvik, T. H., 2014. Plate tectonics in the late Paleozoic. Geoscience Frontiers, 5(3):303–350.

Elburg, M., Vroon, P., van der Wagt, B., and Tchalikian, A., 2005. Sr and Pb isotopic composition of five USGS glasses (BHVO-2G, BIR-1G, BCR-2G, TB-1G, NKT-1G). Chemical Geology, 223(4):196–207.

Flügel, H.W., 1972. Zur Entwicklung der ‘Prototethys’ im Paläozoikum Vorderasiens. N. Jb. Geol. Paläont. Mh. 10, 602–610.

Freeman, S., Inger, S., Butler, R., and Cliff, R., 1997. Dating deformation using Rb/Sr in white mica: Greenschist facies deformation ages from the Entrelor shear zone, Italian Alps. Tectonics, 16(1):57–76.

Fürsich, F., Hautmann, M., Senowbari-Daryan, B., and Seyed-Emami, K., 2005. The Upper Triassic Nayband and Darkuh formations of east-central Iran: Stratigraphy, facies patterns and biota of extensional basins on an accreted terrane. Beringeria, 35:53–133.

Fürsich, F. T., Wilmsen, M., Seyed-Emami, K., and Majidifard, M. R., 2003. Evidence of synsedimentary tectonics in the northern Tabas Block, east-central Iran: the Callovian (Middle Jurassic) Sikhor Formation. Facies, 48(1):151–170.

Fürsich, F. T., Wilmsen, M., Seyed-Emami, K., and Majidifard, M. R., 2009a. Lithostratigraphy of the Upper Triassic–Middle Jurassic Shemshak Group of Northern Iran. Geological Society, London, Special Publications, 312(1):129–160.

Fürsich, F. T., Wilmsen, M., Seyed-Emami, K., and Majidifard, M. R., 2009b. The MidCimmerian tectonic event (Bajocian) in the Alborz Mountains, Northern Iran: evidence of the break-up unconformity of the South Caspian Basin. Geological Society, London, Special Publications, 312(1):189–203.

Gaetani, M., Angiolini, L., Ueno, K., Nicora, A., Stephenson, M. H., Sciunnach, D., Rettori, R., Price, G. D., and Sabouri, J., 2009. Pennsylvanian–Early Triassic stratigraphy in the Alborz Mountains (Iran). Geological Society, London, Special Publications, 312(1):79–128.

Glodny, J., Grauert, B., Fiala, J., Vejnar, Z., and Krohe, A., 1998. Metapegmatites in the western Bohemian massif: ages of crystallisation and metamorphic overprint, as constrained by U–Pb zircon, monazite, garnet, columbite and Rb–Sr muscovite data. Geologische Rundschau, 87(1):124–134.

Glodny, J., Kühn, A., and Austrheim, H., 2008. Diffusion versus recrystallization processes in Rb–Sr geochronology: isotopic relics in eclogite facies rocks, Western Gneiss Region, Norway. Geochimica et Cosmochimica Acta, 72(2):506–525.

Golonka, J., 2004. Plate tectonic evolution of the southern margin of Eurasia in the Mesozoic and Cenozoic. Tectonophysics, 381(1-4):235–273.

Golonka, J. and Gawęda, A., 2012. Plate tectonic evolution of the southern margin of Laurussia in the Paleozoic. Tectonics recent advances. InTech, pages 261–282.

Haghipour, A., Bolourchi, M., Houshmandzadeh, A., Sabzehei, M., Stöcklin, J., Hubber, H., Sluiter, W., and Aghanabati, A., 1977a. Exploration Text of the Ardekan Quderangle map. Geol. Surv. of Iran.) Tehran, Iran.

Haghipour, A. et al., 1977b. Geological map of the Posht-e-Badam area.

Hassanzadeh, J., Stockli, D. F., Horton, B. K., Axen, G. J., Stockli, L. D., Grove, M., Schmitt, A. K., and Walker, J. D., 2008. U-Pb zircon geochronology of late Neoproterozoic– Early Cambrian granitoids in Iran: Implications for paleogeography, magmatism, and exhumation history of Iranian basement. Tectonophysics, 451(1-4):71–96.

Hassanzadeh, J. and Wernicke, B. P., 2016. The Neotethyan Sanandaj-Sirjan zone of Iran as an archetype for passive margin-arc transitions. Tectonics, 35(3):586–621.

Hayden, L. A., Watson, E. B., and Wark, D. A., 2008. A thermobarometer for sphene (titanite). Contributions to Mineralogy and Petrology, 155(4):529–540.

Henry, D. J., Guidotti, C. V., and Thomson, J. A., 2005. The Ti-saturation surface for low-to-medium pressure metapelitic biotites: Implications for geothermometry and Ti substitution mechanisms. American mineralogist, 90(2-3):316–328.

Hogmalm, K. J., Zack, T., Karlsson, A. K.-O., Sjöqvist, A. S., and Garbe-Schönberg, D., 2017. In-situ Rb–Sr and K–Ca dating by LA-ICP-MS/MS: an evaluation of N_2O and SF_6 as reaction gases. Journal of Analytical Atomic Spectrometry, 32(2):305–313.

Holland, T. and Blundy, J., 1994. Non-ideal interactions in calcic amphiboles and their bearing on amphibole-plagioclase thermometry. Contributions to Mineralogy and Petrology, 116(4):433–447.

Holland, T. and Powell, R., 1998. An internally consistent thermodynamic data set for phases of petrological interest. Journal of metamorphic Geology, 16(3):309–343.

Holland, T. and Powell, R., 2003. Activity–composition relations for phases in petrological calculations: an asymmetric multicomponent formulation. Contributions to Mineralogy and Petrology, 145(4):492–501.

Holland, T. and Powell, R., 2011. An improved and extended internally consistent thermodynamic dataset for phases of petrological interest, involving a new equation of state for solids. Journal of Metamorphic Geology, 29(3):333–383.

Horton, B., Hassanzadeh, J., Stockli, D., Axen, G., Gillis, R., Guest, B., Amini, A., Fakhari, M., Zamanzadeh, S., and Grove, M., 2008. Detrital zircon provenance of Neoproterozoic to Cenozoic deposits in Iran: Implications for chronostratigraphy and collisional tectonics. Tectonophysics, 451(1-4):97–122.

Jager, E., Niggli, E., and Wenk, E., 1967. Rb/Sr Altersbestimmungen an Glimmern der Zentralalpen. Kummerly & Frey.

Javadi, H. R., Esterabi Ashtiani, M., Guest, B., Yassaghi, A., Ghassemi, M. R., Shahpasandzadeh, M., and Naeimi, A., 2015. Tectonic reversal of the western Doruneh fault system: implications for Central Asian tectonics. Tectonics, 34(10):2034–2051.

Javadi, H. R., Ghassemi, M. R., Shahpasandzadeh, M., Guest, B., Ashtiani, M. E., Yassaghi, A., and Kouhpeyma, M., 2013. History of faulting on the Doruneh Fault System: implications for the kinematic changes of the Central Iranian Microplate. Geological Magazine, 150(4):651–672.

Jenkin, G. R., 1997. Do cooling paths derived from mica Rb/Sr data reflect true cooling paths? Geology, 25(10):907–910.

Jenkin, G. R., Ellam, R. M., Rogers, G., and Stuart, F. M., 2001. An investigation of closure temperature of the biotite Rb/Sr system: The importance of cation exchange. Geochimica et Cosmochimica Acta, 65(7):1141–1160.

Jentzer, M., Fournier, M., Agard, P., Omrani, J., Khatib, M. M., & Whitechurch, H., 2017. Neogene to Present paleostress field in Eastern Iran (Sistan belt) and implications for regional geodynamics. Tectonics, 36(2), 321-339.

Jochum, K. P., Nohl, U., Herwig, K., Lammel, E., Stoll, B., and Hofmann, A. W., 2005. GeoReM: a new geochemical database for reference materials and isotopic standards. Geostandards and Geoanalytical Research, 29(3):333–338.

Jochum, K. P., Wilson, S. A., Abouchami, W., Amini, M., Chmeleff, J., Eisenhauer, A., Hegner, E., Iaccheri, L. M., Kieffer, B., Krause, J., et al., 2011. GSD-1G and MPIDING reference glasses for in-situ and bulk isotopic determination. Geostandards and Geoanalytical Research, 35(2):193–226.

Jolivet, L., Faccenna, C., Agard, P., Frizon de Lamotte, D., Menant, A., Sternai, P., & Guillocheau, F., 2016. Neo-Tethys geodynamics and mantle convection: from extension to compression in Africa and a conceptual model for obduction. Canadian journal of earth sciences, 53(11), 1190-1204.

Karagaranbafghi, F., Foeken, J., Guest, B., and Stuart, F., 2012. Cooling history of the Chapedony metamorphic core complex, Central Iran: implications for the Eurasia–Arabia collision. Tectonophysics, 524:100–107.

Kargaranbafghi, F., Neubauer, F., and Genser, J., 2015. Rapid Eocene extension in the Chapedony metamorphic core complex, Central Iran: Constraints from $^{40}Ar/^{39}Ar$ dating. Journal of Asian earth sciences, 106:156–168.

Kargaranbafghi, F., Neubauer, F., Genser, J., Faghih, A., and Kusky, T., 2012. Mesozoic to Eocene ductile deformation of western Central Iran: From Cimmerian collisional orogeny to Eocene exhumation. Tectonophysics, 564:83–100.

Kohn, M. J., 2017. Titanite petrochronology. Reviews in Mineralogy and Geochemistry, 83(1):419–441.

Mahmoudi, S., Masoudi, F., Corfu, F., and Mehrabi, B., 2010. Magmatic and metamorphic history of the Deh-Salm metamorphic Complex, Eastern Lut block, (Eastern Iran), from U–Pb geochronology. International Journal of Earth Sciences, 99(6):1153–1165.

Malekpour-Alamdari, A., Axen, G., Heizler, M., and Hassanzadeh, J., 2017. Largemagnitude continental extension in the northeastern Iranian Plateau: Insight from K-feldspar $^{40}Ar/^{39}Ar$ thermochronology from the Shotor Kuh–Biarjmand metamorphic core complex. Geosphere, 13(4):1207–1233.

Masoodi, M., Yassaghi, A., Sadat, M. A. A. N., Neubauer, F., Bernroider, M., Friedl, G., Genser, J., and Houshmandzadeh, A., 2013. Cimmerian evolution of the Central Iranian basement: Evidence from metamorphic units of the Kashmar–Kerman Tectonic Zone. Tectonophysics, 588:189–208.

Mattei, M., Cifelli, F., Muttoni, G., and Rashid, H., 2015. Post-Cimmerian (Jurassic– Cenozoic) paleogeography and vertical axis tectonic rotations of Central Iran and the Alborz Mountains. Journal of Asian Earth Sciences, 102:92–101.

Metcalfe, I., 2021. Multiple Tethyan Ocean basins and orogenic belts in Asia. Gondwana Res. 1:12.

Moghadam, H. S., Li, Q., Griffin, W., Stern, R., Ishizuka, O., Henry, H., Lucci, F., O'Reilly, S., and Ghorbani, G., 2020. Repeated magmatic buildup and deep "hot zones" in continental evolution: The Cadomian crust of Iran. Earth and Planetary Science Letters, 531:115989.

Moghadam, H. S., Li, X.-H., Griffin, W. L., Stern, R. J., Thomsen, T. B., Meinhold, G., Aharipour, R., and O'Reilly, S. Y., 2017. Early Paleozoic tectonic reconstruction of Iran: tales from detrital zircon geochronology. Lithos, 268:87–101.

Moghadam, H. S., Li, X.-H., Ling, X.-X., Stern, R. J., Khedr, M. Z., Chiaradia, M., Ghorbani, G., Arai, S., and Tamura, A., 2015. Devonian to Permian evolution of the Paleo-Tethys Ocean: new evidence from U–Pb zircon dating and Sr–Nd–Pb isotopes of the Darrehanjir– Mashhad "ophiolites", NE Iran. Gondwana Research, 28(2):781–799.

Molina, J., Moreno, J., Castro, A., Rodríguez, C., and Fershtater, G., 2015. Calcic amphibole thermobarometry in metamorphic and igneous rocks: New calibrations based on plagioclase/amphibole Al-Si partitioning and amphibole/liquid Mg partitioning. Lithos, 232:286–305.

Muttoni, G., Gaetani, M., Kent, D. V., Sciunnach, D., Angiolini, L., Berra, F., Garzanti, E., Mattei, M., and Zanchi, A., 2009a. Opening of the Neo-Tethys Ocean and the Pangea B to Pangea A transformation during the Permian. GeoArabia, 14(4):17–48.

Muttoni, G., Mattei, M., Balini, M., Zanchi, A., Gaetani, M., and Berra, F., 2009b. The drift history of Iran from the Ordovician to the Triassic. Geological Society, London, Special Publications, 312(1):7–29.

Omrani, H., Moazzen, M., Oberhänsli, R., Tsujimori, T., Bousquet, R., and Moayyed, M., 2013. Metamorphic history of glaucophane-paragonite-zoisite eclogites from the Shanderman area, northern Iran. Journal of Metamorphic Geology, 31(8):791–812.

Paton, C., Hellstrom, J., Paul, B., Woodhead, J., and Hergt, J., 2011. Iolite: Freeware for the visualisation and processing of mass spectrometric data. Journal of Analytical Atomic Spectrometry, 26(12):2508–2518.

Paton, C., Woodhead, J. D., Hellstrom, J. C., Hergt, J. M., Greig, A., and Maas, R., 2010. Improved laser ablation U-Pb zircon geochronology through robust downhole fractionation correction. Geochemistry, Geophysics, Geosystems, 11(3):1-36.

Paul, A., Hatzfeld, D., Kaviani, A., Tatar, M., and Péquegnat, C., 2010. Seismic imaging of the lithospheric structure of the Zagros mountain belt (Iran). Geological Society, London, Special Publications, 330(1):5–18.

Pouchou, J.-L. and Pichoir, F., 1991. Quantitative analysis of homogeneous or stratified microvolumes applying the model “PAP”. In Electron probe quantitation, pages 31–75. Springer.

Powell, R., Green, E. C., Marillo Sialer, E., and Woodhead, J., 2020. Robust isochron calculation. Geochronology, 2(2):325–342.

Purdy, J. and Jäger, E., 1976. K-Ar ages on rock-forming minerals from the Central Alps: Memorie degli Instituti di Geologia e Mineralogia dell’Universitá di Padova, v. 30.

Rahmati-Ilkhchi, M., Faryad, S. W., Holub, F. V., Košler, J., and Frank, W., 2011. Magmatic and metamorphic evolution of the Shotur Kuh metamorphic complex (Central Iran). International Journal of Earth Sciences, 100(1):45–62.

Rahmati-Ilkhchi, M., Jeřábek, P., Faryad, S. W., and Koyi, H. A., 2010. Mid-Cimmerian, Early Alpine and Late Cenozoic orogenic events in the Shotur Kuh metamorphic complex, Great Kavir block, NE Iran. Tectonophysics, 494(1-2):101–117.

Ramezani, J. and Tucker, R. D., 2003. The Saghand region, central Iran: U-Pb geochronology, petrogenesis and implications for Gondwana tectonics. American journal of science, 303(7):622–665.

Rossetti, F., Monié, P., Nasrabady, M., Theye, T., Lucci, F., and Saadat, M., 2017. Early Carboniferous subduction-zone metamorphism preserved within the Palaeo-Tethyan Rasht ophiolites (western Alborz, Iran). Journal of the Geological Society, 174(4):741–758.

Rossetti, F., Nasrabady, M., Vignaroli, G., Theye, T., Gerdes, A., Razavi, M. H., and Vaziri, H. M., 2010. Early Cretaceous migmatitic mafic granulites from the Sabzevar range (NE Iran): implications for the closure of the Mesozoic peri-Tethyan oceans in central Iran. Terra Nova, 22(1):26–34.

Rossetti, F., Nozaem, R., Lucci, F., Vignaroli, G., Gerdes, A., Nasrabadi, M., and Theye, T., 2015. Tectonic setting and geochronology of the Cadomian (Ediacaran-Cambrian) magmatism in central Iran, Kuh-e-Sarhangi region (NW Lut Block). Journal of Asian Earth Sciences, 102:24–44.

Ruttner, A., 1993. Southern borderland of Triassic Laurasia in north-east Iran. Geologische Rundschau, 82(1):110–120.

Ruttner, A. W., Brandner, R., and Kirchner, E., 1991. Geology of the Aghdarband area (Kopet Dagh, NE-Iran). Abhandlungen der Geologischen Bundesanstalt, 38:7–79.

Salehi, M. A., Moussavi-Harami, R., Mahboubi, A., Fürsich, F. T., Wilmsen, M., and Heubeck, C., 2018. A tectono-stratigraphic record of an extensional basin: the Lower Jurassic Ab-Haji Formation of east-central Iran. Swiss Journal of Geosciences, 111(1):51– 78.

Schärer, U., & Labrousse, L., 2003. Dating the exhumation of UHP rocks and associated crustal melting in the Norwegian Caledonides. Contributions to Mineralogy and Petrology, 144(6), 758-770.

Schoene, B. and Bowring, S. A., 2006. U-Pb systematics of the McClure Mountain syenite: thermochronological constraints on the age of the $^{40}Ar/^{39}Ar$ standard MMhb. Contributions to Mineralogy and Petrology, 151(5):615.

Şengör, A.M.C., 1979. Mid-Mesozoic closure of Permo-Triassic Tethys and its implications. Nature 279, 590–593.

Sengör, A. C., 2012. Tectonic evolution of the Tethyan region (Vol. 259). Springer Science & Business Media.

Seyed-Emami, K. and Alavi-Naini, M., 1990. Bajocian stage in iran. Mem. descr. carta goel. Ital, 40:215–222.

Sheikholeslami, M. and Kouhpeyma, M., 2012. Structural analysis and tectonic evolution of the eastern Binalud Mountains, NE Iran. Journal of Geodynamics, 61:23–46.

Smith, R. B., 1979. The influence of mountains on the atmosphere. In Advances in geophysics (Vol. 21, pp. 87-230). Elsevier.

Soffel, H., Schmidt, S., Davoudzadeh, M., and Rolf, C., 1996. New palaeomagnetic data from Central Iran and a Triassic palaeoreconstruction. Geologische Rundschau, 85(2):293–302.

Soleimani, M., Faghih, A., and Kusky, T., 2021. Mesozoic compressional to extensional tectonics in the Central East Iranian Microcontinent: evidence from the Boneh Shurow metamorphic core complex. Journal of the Geological Society.

Spandler, C., Hammerli, J., Sha, P., Hilbert-Wolf, H., Hu, Y., Roberts, E., and Schmitz, M., 2016. MKED1: a new titanite standard for in-situ analysis of Sm–Nd isotopes and U–Pb geochronology. Chemical Geology, 425:110–126.

Stampfli, G. M. and Borel, G., 2002. A plate tectonic model for the Paleozoic and Mesozoic constrained by dynamic plate boundaries and restored synthetic oceanic isochrons. Earth and Planetary Science Letters, 196(1-2):17–33.

Stille, H., 1924. Grundfragen der vergleichenden Tektonik. Gebrüder Borntraeger.

Stille, H., 1958. Die assyntische Tektonik im geologischen Erdbild. Beih. Geol. Jb. 22, 255.

Stöcklin, J., 1974. Possible ancient continental margins in Iran. In The geology of continental margins, pages 873–887. Springer.

Stöcklin, J., 1968. Structural history and tectonics of Iran: a review. AAPG bulletin, 52(7):1229–1258.

Suess, E., 1895. Note sur l'histoire des oceans. Comptes-Rendus Hebdomadaires de l'Academie des Sciences de Paris. 121, pp. 1113–1116.

Torsvik, T. H. and Cocks, L. R. M., 2016. Earth history and palaeogeography. Cambridge University Press.

Tuttle, O. F. and Bowen, N. L., 1958. Origin of granite in the light of experimental studies in the system $NaAlSi_30_8$-$KAlSi_30_8$-$Si0_2$-H20, volume 74. Geological Society of America.

Verdel, C., Wernicke, B. P., Ramezani, J., Hassanzadeh, J., Renne, P. R., and Spell, T. L., 2007. Geology and thermochronology of Tertiary Cordilleran-style metamorphic core complexes in the Saghand region of central Iran. Geological Society of America Bulletin, 119(7-8):961–977.

Vermeesch, P., 2018. IsoplotR: A free and open toolbox for geochronology. Geoscience Frontiers, 9(5):1479–1493.

Verschure, R., Andriessen, P., Boelrijk, N., Hebeda, E., Maijer, C., Priem, H., and Verdurmen, E. T., 1980. On the thermal stability of Rb/Sr and K-Ar biotite systems: evidence from coexisting Sveconorwegian (ca 870 Ma) and Caledonian (ca 400 Ma) biotites in SW Norway. Contributions to Mineralogy and Petrology, 74(3):245–252.

Villa, I. M., 2010. Disequilibrium textures versus equilibrium modelling: geochronology at the crossroads. Geological Society, London, Special Publications, 332(1):1–15.

Villa, I. M., De Bièvre, P., Holden, N., and Renne, P., 2015. IUPAC-IUGS recommendation on the half-life of ^{87}Rb. Geochimica et Cosmochimica Acta, 164:382–385.

Wendt, J., Kaufmann, B., Bełka, Z., Farsan, N., and Bavandpurs, A. K., 2005. Devonian/Lower Carboniferous stratigraphy, facies patterns and palaeogeography of Iran Part II. Northern and central Iran. Acta geologica polonica, 55(1):31–97.

Wensink, H. et al., 1979. The implications of some palaeomagnetic data from Iran for its structural history.

White, R., Powell, R., Holland, T., Johnson, T., and Green, E., 2014. New mineral activity–composition relations for thermodynamic calculations in metapelitic systems. Journal of Metamorphic Geology, 32(3):261–286.

White, R., Powell, R., Holland, T., and Worley, B., 2000. The effect of TiO_2 and Fe_2O_3 on metapelitic assemblages at greenschist and amphibolite facies conditions: mineral equilibria calculations in the system K_2O-FeO-MgO-Al_2O_3-SiO_2-H_2O-TiO_2-Fe_2O_3. Journal of Metamorphic Geology, 18(5):497–511.

Whitney, D. L. and Evans, B. W., 2010. Abbreviations for names of rock-forming minerals. American mineralogist, 95(1):185–187.

Wilmsen, M., Fürsich, F. T., and Majidifard, M. R., 2015. An overview of the Cretaceous stratigraphy and facies development of the Yazd Block, western Central Iran. Journal of Asian Earth Sciences, 102:73–91.

Wilmsen, M., Fürsich, F. T., and Seyed-Emami, K., 2003. Revised lithostratigraphy of the Middle and Upper Jurassic Magu Group of the northern Tabas Block, east-central Iran. Newsletters on Stratigraphy, pages 143–156.

Wilmsen, M., Fürsich, F. T., Seyed-Emami, K., and Majidifard, M. R., 2009a. An overview of the stratigraphy and facies development of the Jurassic System on the Tabas Block, east-central Iran. Geological Society, London, Special Publications, 312(1):323–343.

Wilmsen, M., Fürsich, F. T., Seyed-Emami, K., and Majidifard, M. R., 2021. The Upper Jurassic Garedu Red Bed Formation of the northern Tabas Block: elucidating Late Cimmerian tectonics in east-Central Iran. International Journal of Earth Sciences, 110(3):767– 790.

Wilmsen, M., Fürsich, F. T., Seyed-Emami, K., Majidifard, M. R., and Taheri, J., 2009b. The Cimmerian Orogeny in northern Iran: Tectono-stratigraphic evidence from the foreland. Terra Nova, 21(3):211–218.

Wilmsen, M., Fürsich, F. T., Seyed-Emami, K., Majidifard, M. R., and Zamani-Pedram, M., 2010. Facies analysis of a large-scale Jurassic shelf-lagoon: the Kamar-e-Mehdi Formation of east-central Iran. Facies, 56(1):59.

Wilmsen, M., Fürsich, F. T., and Taheri, J., 2009c. The Shemshak Group (Lower–Middle Jurassic) of the Binalud Mountains, NE Iran: stratigraphy, depositional environments and geodynamic implications. Geological Society, London, Special Publications, 312(1):175–188.

Wilmsen, M., Wiese, F., Seyed-Emami, K., and Fürsich, F. T., 2005. First record and significance of Turonian ammonites from the Shotori Mountains, east-central Iran. Cretaceous Research, 26(2):181–195.

Wu, C.-M. and Chen, H.-X., 2015. Revised Ti-in-biotite geothermometer for ilmenite-or rutile-bearing crustal metapelites. Science Bulletin, 60(1):116–121.

Yang, P. and Rivers, T., 2000. Trace element partitioning between coexisting biotite and muscovite from metamorphic rocks, Western Labrador: Structural, compositional and thermal controls. Geochimica et Cosmochimica Acta, 64(8):1451–1472.

Zack, T. and Hogmalm, K. J., 2016. Laser ablation Rb/Sr dating by online chemical separation of Rb and Sr in an oxygen-filled reaction cell. Chemical Geology, 437:120–133.

Zanchetta, S., Berra, F., Zanchi, A., Bergomi, M., Caridroit, M., Nicora, A., and Heidarzadeh, G., 2013. The record of the Late Palaeozoic active margin of the Palaeotethys in NE Iran: constraints on the Cimmerian orogeny. Gondwana Research, 24(3-4):1237– 1266.

Zanchetta, S., Malaspina, N., Zanchi, A., Benciolini, L., Martin, S., Javadi, H., and Kouhpeyma, M., 2018. Contrasting subduction–exhumation paths in the blueschists of the Anarak Metamorphic Complex (Central Iran). Geological Magazine, 155(2):316–334.

Zanchetta, S., Zanchi, A., Villa, I., Poli, S., and Muttoni, G., 2009. The Shanderman eclogites: a Late Carboniferous high-pressure event in the NW Talesh Mountains (NW Iran). Geological Society, London, Special Publications, 312(1):57–78.

Zanchi, A., Malaspina, N., Zanchetta, S., Berra, F., Benciolini, L., Bergomi, M., Cavallo, A., Javadi, H. R., and Kouhpeyma, M., 2015. The Cimmerian accretionary wedge of Anarak, Central Iran. Journal of Asian Earth Sciences, 102:45–72.

Zanchi, A., Zanchetta, S., Balini, M., and Ghassemi, M. R., 2016. Oblique convergence during the Cimmerian collision: evidence from the Triassic Aghdarband Basin, NE Iran. Gondwana Research, 38:149–170.

Zanchi, A., Zanchetta, S., Berra, F., Mattei, M., Garzanti, E., Molyneux, S., Nawab, A., and Sabouri, J., 2009a. The Eo-Cimmerian (Late? Triassic) orogeny in North Iran. Geological Society, London, Special Publications, 312(1):31–55.

Zanchi, A., Zanchetta, S., Garzanti, E., Balini, M., Berra, F., Mattei, M., and Muttoni, G., 2009b. The Cimmerian evolution of the Nakhlak–Anarak area, Central Iran, and its bearing for the reconstruction of the history of the Eurasian margin. Geological Society, London, Special Publications, 312(1):261–286.

Ziegler, P. A., 1992. Plate tectonics, plate moving mechanisms and rifting. Tectonophysics, 215(1-2), 9-34.

Ziegler, W. H., 1975. Outline of the Geological History of the North Sea. WOODLAND, A. W. (ed.) Proceedings of the 4th Conference on Petroleum Geology, Petroleum and the Continental Shelf of North-west Europe, 1:131–149.

Figure Captions

Figure 1: Simplified geological map of Iran showing the main tectonic subdivisions and locations discussed in the text. Insert showing the Iranian cimmerian blocks and blue lines showing oceanic sutures. Ophiolites are shown in pink and intrusive and volcanic rocks in red. Metamorphic complex related to the Paleotethys closure in green areas. KKTZ=Kashmar-Kerman Tectonic Zone, AMC&JMC=Anarak and Jandaq Metamorphic complexes. Modified from Paul et al. 2010.

Figure 2: Geological map of central Iran. Modified from Zanchi et al. (2015).

Figure 3: a,b,c) Configuration of the western Cimmerian blocks from the Cambrian to the Jurassic modified from Torsvik and Cocks (2016) and Wilmsen et al. (2009). d) Paleogeographic situation of the CEIM after the Cimmerian orogeny modified from Salehi et al. (2018). The timeline (Ma) shows the major orogeneses and oceans affecting the Cimmerian blocks as well as the metamorphic events affecting Central Iran (References in text).

Figure 4: Simplified geological map of the Kashmar-Kerman Tectonic Zone with localization of samples and cross sections. Modified from Ramezani and Tucker (2003) and Haghipour et al. (1977).

Figure 5: (a) Panorama of part of Sarkuh complex showing large folded marble layers. Microphotographs of samples from the Sarkuh complex of (b) millimetric garnet and staurolite with biotite in their pressure zones, (c) centimetric zoned staurolite with garnet inclusion and biotite in

pressure zone (d) millimetric prismatic sillimanite associated with biotite, (e) centimetric andalusite grains partly replaced by sillimanite, biotite and garnet and (f) zoned garnet replaced by pumpellyite and biotite.

Figure 6: (a) Composition of garnets in a Grs vs Sps diagram and in a Sps+Grs-Alm-Prp ternary diagram. (b) Composition of white micas in a 2Al vs SiFeMg diagram. (c) Composition of biotites in a XMg vs Ti diagram.

Figure 7: Boneh-Shurow complex. (a) Deformation in gneisses with migmatization from the area 1. (b) Augen gneiss with large phenocrystals of K-feldspar from the area 1. (c) K-feldspar rich layers in the gneiss from area 1. SEM pictures of gneiss samples from the area 1 of (d) garnet with titanite inclusions and (e) Bt+Qz+Pl and Amp+Ttn+Grt layers.(f,g) SEM pictures of sample IC1824 from area 2 showing a highly deformed garnet with helicoidal texture and sillimanite inclusions. (h) Pseudomorphosis of Andalusite into kyanite from area 2. (i) SEM picture of a large round grain of K-feldspar from sample IC1824c with inclusions of biotite and quartz and albite exsolutions.

Figure 8: SEM pictures and microphotographs of samples of (a) an amphibolite with biotite and titanite overgrowing ilmenite from the Tashk complex and (b) potentially inherited phlogopite and automorph K-feldspar in a carbonate; (c) cocrystalized chloritoid and white mica from the Jandaq complex; (d) cocrystalized biotite and sillimanite in equilibrium with garnet, (e) staurolite and biotite overgrowing garnets and (f) late euhedral and zoned tourmaline from the Posht-e-Badam complex.

Figure 9: pseudosection of samples IC1915g, IC1828a, IC1824c and AN26d from the Sarkuh, Poshte-Badam, Boneh-Shurow and Jandaq complexes respectively.

Figure 10: U-Pb isochrons of titanites with 2σ uncertainties and Zr content in ppm with data plotted on the colour gradient scale. Tera-Wasserburg plots of titanite petrochronological data. Lower intercept ages are calculated using the robust regression of Powell et al. (2020) and reported at 2SE with s the spine width. Diagrams generated using the ChrontouR package (Larson 2020; doi:10.17605/OSF.IO/P46MB) written for the open R software environment.

Figure 11a: Biotite Rb/Sr dates with 2σ uncertainties from the Jandaq, Chapedony, Poshteh-Badam and Boneh-Shurow complexes.

Figure 11b: Biotite Rb/Sr dates with 2σ uncertainties from the Boneh-Shurow, Tashk and Sarkuh complexes.

Figure 11c: Biotite Rb/Sr ages with 2σ uncertainties from the Sarkuh complex.

Figure 12: Summary of P-T peak conditions from this study with peak conditions from Shotor-Kuh (Rahmati-Ilkhchi et al., 2011); Anarak (Zanchetta et al., 2018) and Rasht blueschists (Rossetti et al., 2015).

Figure 13: This study ages with 2σ bar from the Jandaq and KKTZ metamorphic complexes associated with biotite temperature of crystallization from Ti in biotite (Henry et al., 2005). Same order of samples as in Table 3, poorly constrained ages of IC1812a, IC1915g and IC1913a are excluded. Ages from the literature are also summarized on the left part, see text and table 1 for further details.

Figure 14: Geodynamic model for Central-East Iran during the Jurassic, with the Cimmerian main orogeny ~200 Ma, followed by back-arc rifting ~180 Ma and development of the Caspian Sea ~165 Ma. Large scale strike slip movements later brought together the MP-HT rocks of the Jandaq and the KKTZ complexes.

Tables

Table 1: Geochronological data (2σ) from the Kashmar-Kerman Tectonic Zone in Central Iran.

Table 2: Samples nature, mineralogy (+quartz, +feldspar, + Fe-oxides), localization and mineral composition. Mineral abbreviations are after Whitney and Evans (2010).

Table 3: Rb-Sr dating with biotite temperatures based on Ti content (Henry et al. 2005), Si content of white mica and micas textural relationships with mineral abbreviations after Whitney and Evans (2010).

Rock	Method and dated mineral	Age and error (Ma)	Interpretation	Author(s)
		Western domain		
Daranjir diorite	U–Pb zircon TIMS	43.4±0.2	Intrusion	Ramezani and Tucker (2003)
Khoshoumi granite	U–Pb zircon TIMS	44.3±1.1	Intrusion	Ramezani and Tucker (2003)
Chapedony phorphyroblastic gneiss	U–Pb zircon TIMS	52±9	Intrusion	Ramezani and Tucker (2003)
Chapedony biotite-gneiss	U–Pb zircon TIMS	46.8±2.5	Intrusion	Ramezani and Tucker (2003)
Chapedony migmatite	U–Pb zircon TIMS	46.3±1.7	Intrusion	Ramezani and Tucker (2003)
Khoshoumi volcanic rocks	Ar-Ar biotite	41.2±2.4	Lava extrusion	Verdel et al. (2007)
Khoshoumi dacite	Ar-Ar plagioclase	42.0±1.8	Lava extrusion	Verdel et al. (2007)
Khoshoumi dacite	Ar-Ar K-feldspar	40.5±2.5	Lava extrusion	Verdel et al. (2007)
Neybaz Mt. Mylonitic gneiss	U–Pb zircon TIMS	49.0±0.1	Intrusion	Verdel et al. (2007)
Chapedony granitic dyke	Ar-Ar white mica	42.8±0.6	Cooling age	Kargaranbafghi et al. (2012)
Chapedony hornblende granite	Ar-Ar hornblende	46.4±0.4	Cooling age	Kargaranbafghi et al. (2012)
Chapedony hornblende granite	Ar-Ar K-feldspar	43.8±1.4	Cooling age	Kargaranbafghi et al. (2012)
Chapedony mylonitic granite	Ar-Ar biotite	45.7±0.6	Cooling age	Kargaranbafghi et al. (2012)
Chapedony mylonitic granite	Ar-Ar K-feldspar	42.7±0.2	Cooling age	Kargaranbafghi et al. (2012)
Chapedony granitic gneiss	Ar-Ar biotite	45.6±1.4	Cooling age	Kargaranbafghi et al. (2012)
Chapedony sample	Ar-Ar biotite	49.1±1.0	Cooling age	Kargaranbafghi et al. (2012)
Chapedony subvolanic dyke	Ar-Ar hornblende	45.4±0.4	Cooling age	Kargaranbafghi et al. (2012)
Chapedony subvolanic dyke	Ar-Ar K-feldspar	44.0±0.4	Cooling age	Kargaranbafghi et al. (2012)
Chapedony hornblende granodiorite	Ar-Ar biotite	40.0±1.2	Cooling age	Kargaranbafghi et al. (2012)
Chapedony biotite gneiss	Ar-Ar biotite	41.9±0.8	Cooling age	Kargaranbafghi et al. (2012)
Chapedony biotite gneiss	Ar-Ar hornblende	47.6±1.0	Cooling age	Kargaranbafghi et al. (2015)
Chapedony mylonitic granodiorite	Ar-Ar biotite	43.1±1.8	Cooling age	Kargaranbafghi et al. (2015)
Chapedony mylonitic granodiorite	Ar-Ar hornblende	45.3±1.2	Cooling age	Kargaranbafghi et al. (2015)
Chapedony mylonitic granodiorite	Ar-Ar K-feldspar	42.7±1.6	Cooling age	Kargaranbafghi et al. (2015)
Kuh-e-Neybaz mylonite	Ar-Ar white mica	43.1±0.8	Shear zone activity	Kargaranbafghi et al. (2015)
Kuh-e-Neybaz augen gneiss	Ar-Ar biotite	41.3±1.4	Cooling after metamorphism	Kargaranbafghi et al. (2015)
Kuh-e-Neybaz gneiss	Ar-Ar biotite	46.7±1.6	Cooling after metamorphism	Kargaranbafghi et al. (2015)
Khoshoumi granite	Ar-Ar K-feldspar	44.4±0.6	Cooling after intrusion	Kargaranbafghi et al. (2015)
		Central domain		
NW Kuh-e-Chamgou metarhyolite	K–Ar whole rock	170 ±11	Cooling after metamorphism	Aistov et al. (1984)
Chamgo granodiorite	U–Pb zircon TIMS	213.5±0.5	Intrusion	Ramezani and Tucker (2003)
Esmail-Abad granite	U–Pb zircon TIMS	218.0±3.2	Intrusion	Ramezani and Tucker (2003)
Esmail-Abad ophiolitic melange	Ar-Ar hornblende	187.6±1.8	Intrusion	Bagheri and Stampfli (2008)
Posht-e-Badam silicate marble	Ar-Ar white mica	220.5±0.5	Cooling after metamorphism	Kargaranbafghi et al. (2012)
Posht-e-Badam silicate marble	Ar-Ar white mica	45.5±0.6	Cooling after metamorphism	Kargaranbafghi et al. (2012)
Posht-e-Badam retrogressed gneiss	Ar-Ar white mica	55.4±0.6	Cooling after metamorphism	Kargaranbafghi et al.(2012)
Posht-e-Badam granodiorite	Ar-Ar hornblende	219.2±2.4	Metamorphism	Kargaranbafghi et al. (2012)
Posht-e-Badam quartz phyllonite	Ar-Ar white mica	180.9±1.4	Cooling after metamorphism	Kargaranbafghi et al. (2012)
Posht-e-Badam complex phyllite	Ar-Ar white mica	93.6±1.6	Cooling through ca. 400 °c	Kargaranbafghi et al. (2015)
		Eastern domain		
Tashk formation volcanoclastic tuff	U–Pb zircon TIMS	627±19	Younger detrital zircon	Ramezani and Tucker (2003)
Zarigan leucogranite (S)	U–Pb zircon TIMS	529±16	Intrusion	Ramezani and Tucker (2003)
Zarigan leucogranite (S)	U–Pb zircon TIMS	784±69	Intrusion	Ramezani and Tucker (2003)
Douzak-Darreh leucogranite (S)	U–Pb zircon TIMS	525.7±1.0	Intrusion	Ramezani and Tucker (2003)
Rhyolite of Cambrian volcanosedimentary unit	U–Pb zircon TIMS	528.2±0.8	Lava extrusion	Ramezani and Tucker (2003)
Dacite-porphyry of Cambrian volcanosedimentary unit (S)	U–Pb zircon TIMS	527.9±1.0	Lava extrusion	Ramezani and Tucker (2003)
Polo Mt. granodiorite	U–Pb zircon TIMS	530±21	Intrusion	Ramezani and Tucker (2003)
Ariz Mt. Granodiorite	U–Pb zircon TIMS	533±1	Intrusion	Ramezani and Tucker (2003)
Boneh Shurow granitic gneiss (Saghand)	U–Pb zircon TIMS	544±7	Intrusion	Ramezani and Tucker (2003)
Boneh Shurow garnet-amphibolite	U–Pb zircon TIMS	547.6±2.0	Metamorphism	Ramezani and Tucker (2003)
Boneh Shurow quartz-diorite	U–Pb zircon TIMS	547.0±2.5	Intrusion	Ramezani and Tucker (2003)
Boneh Shurow granitic gneiss	U–Pb zircon TIMS	544.4±6.7	Intrusion	Verdel et al. (2007)
Boneh Shurow schist	Ar-Ar biotite	149.75±0.5	Cooling after metamorphism	Verdel et al. (2007)
Boneh Shurow metapelitic schist	Ar-Ar biotite	156.9±0.6	Cooling after metamorphism	Verdel et al. (2007)
Boneh Shurow	Ar-Ar biotite	159.6±0.6	Cooling after metamorphism	Verdel et al. (2007)
Tashk formation	Ar-Ar biotite	218.3±0.5	Cooling after metamorphism	Verdel et al. (2007)
Tashk formation graywacke	Ar-Ar biotite	295.4±1.1	Cooling after metamorphism	Verdel et al. (2007)
Tashk formation	Ar-Ar biotite	281.3±1.2	Cooling after metamorphism	Verdel et al. (2007)
Boneh Shurow Reato-Liassic phyllite	Ar-Ar white mica	140.8±0.6	Low grade metamorphism	Kargaranbafghi et al. (2012)
Boneh Shurow granodiorite	Ar-Ar biotite	120.1±2.4	Cooling age	Kargaranbafghi et al. (2012)
Boneh Shurow granodiorite	Ar-Ar hornblende	355.5±5.2	Minimum cooling age	Kargaranbafghi et al. (2012)
Boneh Shurow garnet-amphibolite	Ar-Ar hornblende	175.8±2.0	Cooling after metamorphism	Masoodi et al. (2013)
Boneh Shurow granitic gneiss	Ar-Ar white mica	165.5±1.0	Deformation related cooling age	Masoodi et al. (2013)
Boneh Shurow garnet-amphibolite	Ar-Ar biotite	149.0±1.0	Cooling after metamorphism	Masoodi et al. (2013)
Boneh Shurow meta-quartz-diorite	Ar-Ar K-feldspar	115.9±2.6	Cooling age	Masoodi et al. (2013)
Boneh Shurow granitic gneiss	Ar-Ar K-feldspar	129.1±0.8	Cooling age	Masoodi et al. (2013)
Posht-e-Sorkh mylonitic schist	Ar-Ar white mica	168.6±1.2	Shear zone cooling age	Masoodi et al. (2013)
Posht-e-Sorkh mylonitic schist	Ar-Ar white mica	167.7±1.0	Shear zone cooling age	Masoodi et al. (2013)
Posht-e-Sorkh mylonitic biotite gneiss	Ar-Ar biotite	230.4±1.8	Shear zone cooling age	Masoodi et al. (2013)
Posht-e-Sorkh mylonitic garnet-biotite gneiss	Ar-Ar biotite	168.1±1.6	Shear zone cooling age	Masoodi et al. (2013)
Posht-e-Sorkh mylonitic schist	Ar-Ar biotite	182.9±1.6	Shear zone cooling age	Masoodi et al. (2013)
Posht-e-Sorkh mylonitic biotite gneiss	Ar-Ar biotite	197.2±1.6	Shear zone cooling age	Masoodi et al. (2013)
Posht-e-Sorkh mylonitic biotite gneiss	Ar-Ar K-feldspar	191.1±1.2	Shear zone cooling age	Masoodi et al. (2013)
Posht-e-Sorkh mylonitic biotite gneiss	Ar-Ar K-feldspar	186.1±1.6	Shear zone cooling age	Masoodi et al. (2013)
Posht-e-Sorkh mylonitic garnet-biotite gneiss	Ar-Ar K-feldspar	167.9±1.4	Shear zone cooling age	Masoodi et al. (2013)

Table 1

			Mineral																	GPS coordinates		Grt (core-rim)					Ph		Bt		St
Zone	Samples	Lithology	Grt	St	Bt	Ph	Amp	Ep	Cld	And	Ky	Sil	Or	Tur	Ttn	Pmp	Chl	Cb	Ap	LONGITUDE	LATITUDE	Alm	Prp	Sps	Grs	XMg	X_{Mg}	Si pfu	X_{Mg}	Ti pfu	X_{Mg}
Jandaq	JA17b	Micaschist	x	x	x	x											x			54.21025	33.82339	83-81	11-12	1-2	5	0.11-0.12	0.45-0.57	2.97-3.07	0.36-0.39	0.08-0.11	0.07-0.09
	JA26	Micaschist				x		x	x											54.57128	34.00672						0.27-0.35	3.08-3.13			
	JA28b	Micaschist	x	x	x	x											x			54.56811	33.96711	79-84	8-10	8-1	7-5	0.09-0.11	0.37-0.56	3.04-3.10	0.41-0.49	0.03-0.17	0.09-0.12
Chapedony	CH1823	Gneiss			x								x	x						55.09092	32.52186								0.42-0.55	0.05-0.19	
	CH1842	Micaschist			x								x							55.10728	32.50481								0.44-0.50	0.16-0.21	
Posht-e-Badam	PB1828a	Micaschist	x	x	x	x					x	x								55.37764	32.95903	65-81	7-10	23-5	4-6	0.09-0.10	0.39-0.49	2.95-3.05	0.41-0.48	0.09-0.13	0.16-0.19
	PB1828b	Micaschist	x	x	x	x						x								55.37764	32.95903	81-83	9-11	5-2	5-6	0.11-0.12	0.47-0.54	2.97-3.04	0.47-0.49	0.07-0.13	0.17-0.19
	PB1936c	Micaschist	x	x	x	x						x								55.37833	32.95467	73-82	7-10	16-2	5-6	0.09-0.11	0.37-0.46	2.98-3.03	0.43-0.47	0.10-0.13	0.17-0.19
	PB1938	Micaschist	x	x	x	x								x			x			55.37286	32.96125	83-84	10	2-1	5	0.11	0.38-0.47	2.97-3.03	0.35-0.43	0.09-0.18	0.15-0.17
Boneh-Shurow N	BS1837	Gneiss	x					x							x					55.59769	33.04028	-	-	-	-	-					
	BS1947	Gneiss	x		x		x	x							x		x			55.59883	33.03994	55-53	12-15	6-1	31-33	0.16-0.22			0.43-0.46	0.08-0.18	
	BS1952e	Gneiss	x		x		x	x							x		x			55.60722	33.04192	-	-	-	-	-			0.44-0.49	0.12-0.16	
	BS1952g	Gneiss	x		x		x	x					x		x		x			55.60722	33.04192	57-54	3-8	0-1	41-37	0.04-0.10			0.46-0.53	0.05-0.15	
Boneh-Shurow C	BS1824c	Micaschist	x		x	x					x	x	x							55.41244	32.60558	72-85	12-17	16-2	2-3	0.13-0.18	0.51-0.70	3.05-3.15	0.41-0.62	0.13-0.28	
	BS1924	Micaschist	x		x	x					x	x	x	x						55.41292	32.60611	69-71	11-14	16-11	3-4	0.14-0.16	0.54-0.62	3.02-3.07	0.39-0.43	0.11-0.21	
	BS1925	Micaschist	x		x	x				x		x								55.41403	32.60664	76-79	18-17	4-3	1-2	0.20-0.18	0.44-0.66	3.01-3.11	0.41-0.55	0.12-0.17	
	BS1930	Amphibolite	x		x		x								x					55.40803	32.60503	57-62	6-7	10-5	28-26	0.10-0.11			0.37-0.46	0.13-0.20	
Boneh-Shurow S	BS1931	Micaschist	x		x	x														55.35733	32.34019	70-74	14-15	7-3	9-8	0.17-0.18	0.28-0.34	3.01-3.05	0.37-0.56	0.03-0.13	
	BS1933b	Micaschist	x		x	x														55.36078	32.33297	65-68	12-13	15-12	7-9	0.16	0.31-0.34	3.02-3.06	0.50-0.58	0.12-0.15	
	BS1817d	Amphibolite	x		x	x	x										x			55.35856	32.38917	69-70	17	3-2	10-12	0.19-0.20			0.31-0.48	0.08-0.11	
Tashk	TK1802a	Schiste	x		x	x											x			55.51464	32.26028	72-83	5-9	15-0	7-8	0.06-0.10	0.40-0.57	2.96-3.04	0.40-0.42	0.04-0.08	
	TK1802b	Carbonate			x								x		x			x		55.51464	32.26028								0.97-0.98	0.02-0.05	
	TK1802c	Amphibolite			x		x								x					55.51464	32.26028								0.57-0.59	0.12-0.19	
Sarkuh	SK1806a	Amphibolite			x		x													55.55126	32.21813								0.60-0.61	0.18-0.21	
	SK1806b	Micaschist	x		x	x						x	x	x					x	55.55126	32.21813	76-77	12-13	5-3	6-8	0.13-0.15	0.50-0.53	3.08-3.11	0.41-0.51	0.13-0.20	
	SK1808	Micaschist	x	x	x	x														55.56086	32.18825	76-77	9-11	10-7	4-5	0.10-0.13	0.47-0.64	3.07-3.13	0.50-0.59	0.05-0.11	0.14-0.18
	SK1809	Micaschist	x	x	x	x				x		x		x						55.57389	32.18708	75-83	8-9	16-6	1-3	0.09-0.10	0.36-0.55	3.02-3.11	0.34-0.43	0.06-0.18	0.14-0.16
	SK1812a	Micaschist	x		x	x														55.59192	32.24531	79-82	12-11	7-5	2	0.13-0.11	0.44-0.51	3.09-3.10	0.40-0.43	0.15-0.21	
	SK1814	Micaschist	x		x	x					x	x		x						55.58650	32.23917	73-77	13-12	12-7	3-4	0.15-0.14	0.46-0.57	3.02-3.08	0.42-0.46	0.10-0.20	
	SK1903b	Micaschist	x		x												x			55.53892	32.24044	69-75	14-9	11-2	5-13	0.11-0.16			0.54-0.55	0.09-0.10	
	SK1908b	Micaschist	x	x	x	x														55.55831	32.19300	79-82	6-11	8-0	6-8	0.09-0.12	0.45-0.61	2.99-3.13	0.42-0.56	0.05-0.11	0.16-0.20
	SK1910	Micaschist			x												x		x	55.56392	32.19297								0.40-0.60	0.07-0.27	
	SK1911	Micaschist	x	x	x	x														55.56519	32.19225	76-79	10-13	6-1	8-10	0.11-0.14	0.45-0.60	3.05-3.10	0.53-0.58	0.05-0.11	0.18-0.21
	SK1912b	Micaschist	x	x	x	x														55.56553	32.19028	71-79	6-13	18-0	5-9	0.08-0.14	0.50-0.61	3.01-3.13	0.51-0.61	0.06-0.11	0.17-0.22
	SK1913a	Amphibolite	x		x		x	x								x	x		x	55.59917	32.25169	61-54	9-7	17-5	14-33	0.13-0.11			0.45-0.55	0.06-0.21	
	SK1915g	Micaschist	x		x	x					x	x								55.59092	32.24481	80-83	12-10	7-5	1-2	0.13-0.11	0.39-0.48	2.99-3.11	0.26-0.42	0.09-0.22	
	SK1916b	Vein	x		x	x								x						55.58825	32.24294	76-73	8-7	13-17	4-3	0.09-0.08	0.47-0.50	3.05-3.09			
	SK1919	Micaschist	x		x	x														55.57292	32.23033	82-84	14-10	3-2	2-4	0.14-0.10	-	-	0.27-0.31	0.11-0.19	
	SK1923	Micaschist	x		x	x				x		x	x							55.56042	32.22797	67-74	9-10	21-11	3-6	0.13-0.12	0.51-0.57	3.01-3.08	0.39-0.42	0.09-0.21	

Table 2

Table 3

Zone	Samples	biotite ages ±2σ (Ma)	MSWD	Ti T°C	std	white mica ages ±2σ (Ma)	MSWD	Si pheng	std	Micas textural relationships
Jandaq	JA17b	202.0±11.5	2.6	307	31	382.3±86.0	2	3.03	0.08	Ph in pressure zones St, Bt replacing Ph
	JA26					220.3±41.8	1.9	3.12	0.02	Syn Cld
	JA28b	147.9±5.7	2.3	390	87	198.2±16.4	2.4	3.08	0.02	Ph in pressure zones Grt, Bt replacing Ph and Grt
Chapedony	CH1823	42.5±2.0	2.6	554	18					Growth with foliation
	CH1842	42.7±1.8	1.7	555	19					Retrograde
Posht-e-Badam	PB1828a	160.7±2.0	2.9	404	39	227.7±42.3	1.9	2.98	0.02	Bt and Ph syn rim Grt
	PB1828b	159.2±1.9	2.6	353	47	131.8±126.8	1.1	3.01	0.04	Bt and Ph syn rim Grt
	PB1936c	159.4±1.5	2.3	426	27	214.2±30.1	2.1	3.01	0.02	Bt and Ph syn rim Grt
	PB1938	160.5±1.5	2.4	435	26					Bt and Ph post Grt
Boneh-Shurow N	BS1947	141.4±2.3	1.1	467	43					Retrograde
	BS1952e	151.3±2.8	2.7	485	14					Retrograde
	BS1952g	134.7±6.2	2.4	435	56					Retrograde
Boneh-Shurow C	BS1824c	158.0±1.4	2.7	538	30	154.8±32.9	1	3.12	0.02	Composing the matrix, prograde or peak ?
	BS1824c	155.5±3.0	1.5	542	33					Inclusion in K-Feldspar
	BS1924	160.7±2.4	1.2	506	44	198.6±33.2	2.1	3.05	0.01	Composing the matrix, partly retrograde
	BS1925	149.6±1.7	2.5	487	28	170.9±45.8	2.1	3.07	0.03	Ph in pressure zone And, Bt in pressure zone Grt
	BS1930	149.3±7.9	2.8	539	28					Retrograde
Boneh-Shurow S	BS1931	150.1±4.0	2.4	424	40	233.5±21.7	1.3	3.03	0.01	Bt in pressure zone Grt, Ph pre Grt
	BS1933b	159.0±1.7	2	515	14					Bt post Grt, Ph pre Grt
	BS1817d	189.0±25.4	1.2	254	41					Retrograde
Tashk	TK1802a	153.3±3.0	2.6							In pressure zones Grt
	TK1802b	180.5±1.4	2	460	36					Inherited ?
	TK1802c	168.3±2.9	1.3	526	33					Syn Amp et Qz
Sarkuh	SK1806a	172.5±2.4	2.2	617	8					Post/syn Amp
	SK1806b	169.8±2.1	1.7	549	19					In pressure zone Grt
	SK1808	152.7±4.0	2.7	336	37					In pressure zone Grt et St
	SK1809	161.3±3.5	2.2	466	33					In pseudomorph And and Grt and pre/syn Sil
	SK1812a	159.9±2.9	2.7	544	20	455±210	2.1	3.08	0.04	Composing the matrix, prograde or peak ?
	SK1814	168.6±1.7	2.5	540	34	155.7±23.3	1.9	3.04	0.02	Bt and Ph post Ky and pre/syn Sil
	SK1903b	104.0±23.5	3	389	24					Retrograde
	SK1908b	169.7±7.0	1.2	332	68					In pressure zone Grt et St
	SK1910	169.7±3.2	2.2	549	31					Composing the matrix, prograde or peak ?
	SK1911	122.4±11.2	2.5	319	53	125.0±36.7	2.5	3.07	0.02	Bt pressure zone Grt et St, Ph matrix
	SK1912b	161.5±7.9	1.2	286	49					Pressure zone St
	SK1913a	160.2±4.9	2.8	544	22					Syn Amp
	SK1913a	139.6±42.9	1.5	519	24					Retrograde
	SK1915g	172.8±2.4	1.9	534	22	270.2±151.7	2.2	3.04	0.04	Bt and Ph post Ky and pre/syn Sil
	SK1916b					197.1±15.0	2.4	3.06	0.01	Vein
	SK1919	154.5±4.1	2.9	473	36					Post Grt
	SK1923	169.4±2.6	2	553	19					In pseudomorph And and syn Sil

Highlights

- Coupled in-situ Rb/Sr and U/Pb dating allows to constrain metamorphic terranes evolution.
- Iran was affected by a Jurassic collisional metamorphism related to the Paleotethys closure.
- Metamorphic terranes are exhumed from ~170 Ma onward in a context of upper plate extension.

This work is original, has not been published previously and is not under consideration for publication elsewhere. All authors have seen and approved the final version of the manuscript being submitted.

Authors contributions are as follow:

Thomas Gyomlai : Conceptualization, Supervision, Investigation, Methodology, Formal analysis, Writing - Original Draft, Visualization.
Philippe Agard : Conceptualization, Supervision, Writing - Review & Editing, Resources, Funding acquisition.
Laurent Jolivet : Supervision, Writing - Review & Editing, Resources, Funding acquisition.
Tiphaine Larvet : Writing - Review & Editing, Formal analysis, Investigation.
Guillaume Bonnet : Writing - Review & Editing, Validation.
Jafar Omrani : Resources, Funding acquisition.
Kyle Larson : Writing - Review & Editing, Formal analysis, Resources.
Benoit Caron : Methodology, Resources, Validation.
Julie Noël : Formal analysis, Validation.

Declaration of interests

☒ The authors declare that they have no known competing financial interests or personal relationships that could have appeared to influence the work reported in this paper.

☐The authors declare the following financial interests/personal relationships which may be considered as potential competing interests: